Crustal thinning and exhumation along a fossil magma-poor distal margin preserved in Corsica: A hot rift to drift transition?

Crustal thinning and exhumation along a fossil magma-poor distal margin preserved in Corsica: A hot rift to drift transition?

Marco Beltrando[a, b,], Ivan Zibra[c], Alessandra Montanini[d], Riccardo Tribuzio[e, f]

[a] Dipartimento di Scienze della Terra, Università di Torino, Via Valperga Caluso 35, 10125 Torino, Italy

[b] CNRS-EOST, Université de Strasbourg, 1 rue Blessig, 67084 Strasbourg Cedex, France

[c] Geological Survey of Western Australia, Dept. of Mines and Petroleum, 100 Plain Street, East Perth, East Perth, WA 6004, Australia

[d] Dipartimento di Fisica e Scienze della Terra, Università di Parma, Parco Area delle Scienze 157A, 43100 Parma, Italy

[e] Dipartimento di Scienze della Terra e dell'Ambiente, Università di Pavia, Via Ferrata 1, 27100 Pavia, Italy

[f] C.N.R.—Istituto di Geoscienze e Georisorse, Unità Operativa di Pavia, Via Ferrata 1, 27100 Pavia, Italy

Abstract

Rift-related thinning of continental basement along distal margins is likely achieved through the combined activity of ductile shear zones and brittle faults. While extensional detachments responsible for the latest stages of exhumation are being increasingly recognized, rift-related shear zones have never been sampled in ODP sites and have only rarely been identified in fossil distal margins preserved in orogenic belts. Here we report evidence of the Jurassic multi-stage crustal thinning preserved in the Santa Lucia nappe (Alpine Corsica), where amphibolite facies shearing persisted into the rift to drift transition. In this nappe, Lower Permian meta-gabbros to meta-gabbro-norites of the Mafic Complex are separated from Lower Permian granitoids of the Diorite–Granite Complex by a 100–250 m wide shear zone. Fine-grained syn-kinematic andesine + Mg-hornblende assemblages in meta-tonalites of the Diorite–Granite Complex indicate shearing at T = 710 ± 40 °C at P < 0.5 GPa, followed by deformation at greenschist facies conditions. $^{40}Ar/^{39}Ar$ step-heating analyses on amphiboles reveal that shearing at amphibolite facies conditions possibly began at the Triassic–Jurassic boundary and persisted until t < 188 Ma, with the Mafic Complex cooling rapidly at the footwall of the Diorite–Granite Complex at ca. 165.4 ± 1.7 Ma.

Final exhumation to the basin floor was accommodated by low-angle detachment faulting, responsible for the 1–10 m thick damage zone locally capping the Mafic Complex. The top basement surface is onlapped at a low angle by undeformed Mesozoic sandstone, locally containing clasts of footwall rocks. Existing constraints from the neighboring Corsica ophiolites suggest an age of ca. 165–160 Ma for these final stages of exhumation of the Santa Lucia basement.

These results imply that middle to lower crustal rocks can be cooled and exhumed rapidly in the last stages of rifting, when significant crustal thinning is accommodated in less than 5 Myr through the consecutive activity of extensional shear zones and detachment faults. High thermal gradients may

delay the switch from ductile shear zone- to detachment-dominated crustal thinning, thus preventing the exhumation of middle and lower crustal rocks until the final stages of rifting.

1. Introduction

The geometry of magma-poor rifted margins has been increasingly constrained in the last 20 years thanks to studies conducted along present day rifted margins (e.g. Afilhado et al., 2008, Espurt et al., 2012, Péron-Pinvidic and Manatschal, 2009, Whitmarsh and Wallace, 2001, Whitmarsh et al., 2001 and Zhu et al., 2012) and fossil analogues (e.g. Froitzheim et al., 1994, Jammes et al., 2009 and Manatschal, 2004). The resulting picture indicates that crustal thickness decreases from the proximal domain, affected by block faulting and limited crustal stretching, to the Zone of Exhumed Subcontinental Mantle, where continental crust is completely excised. Crustal thinning is accomplished within the distal continental margin, which generally consists of a 'necking zone', where crustal thickness decreases rapidly from ca. 25–30 km to ca. 10 km, followed oceanward by a wide area with < 10 km thick crust (e.g. Mohn et al., 2012 and Osmundsen and Ebbing, 2008).

Despite these significant advances, the dynamics of lithospheric thinning leading to the architecture described above are still poorly understood, since the large scale extensional structures commonly observed in distal margins are related to the final stages of deformation, characterized by low-angle detachment faulting (e.g. Froitzheim and Eberli, 1990, Jammes et al., 2009, Manatschal, 2004 and Whitmarsh and Wallace, 2001). However, several lines of evidence suggest that extensional shear zones should play a key role in accommodating crustal thinning along distal continental margins, decoupling deformation at different crustal levels. Middle to lower crustal decoupling horizons have been advocated based on the bathymetric evolution of Atlantic-type distal margins (e.g. Dupré et al., 2007, Huismans and Beaumont, 2008 and Kusznir and Karner, 2007), where wide regions of extremely attenuated crust are overlain by a thin shallow marine syn-rift sedimentary cover (e.g. Wilson et al., 2001). In these settings, transient isostatic support may be provided by greater thinning of the lower crust and upper mantle with respect to the upper crustal layers, leading to the anomalous shallow bathymetry (Brun and Beslier, 1996, Kusznir and Karner, 2007, Huismans and Beaumont, 2008 and Huismans and Beaumont, 2011). Middle crustal shear zones have also been proposed to account for the apparent lack of upper crustal deformation in the early rift stages despite significant bulk crustal thinning, possibly accommodated in the lower crust (Lavier and Manatschal, 2006). However, rift-related shear zones have only rarely been detected in fossil distal continental margins (Bissig and Hermann, 1999 and Mohn et al., 2012). Therefore, the presence of crustal scale shear zones and their timing of activity with respect to the rifting and drifting evolution awaits to be tested with field studies on fossil margins preserved in orogenic belts and with future IODP's.

In this study we report evidence of multi-stage thinning and cooling of a crustal section from amphibolite facies conditions to the floor of the Western Tethys in the Mesozoic. Our results indicate that amphibolite-facies shear zones can still be active at the rift-to-drift transition and that significant crustal/lithospheric thinning and cooling can be achieved very rapidly at the edge of continental plates in the last stages of rifting.

2. Geological setting

The Santa Lucia nappe is located in the northern part of Corsica (France), in the Western Mediterranean area (Fig. 1). The island originally represented the south-western continuation of the Western Alps and of its European foreland (e.g. Molli, 2008), prior to counter-clockwise rotation that initiated at ca. 30 Ma (e.g. Speranza et al., 2002). The domain that largely escaped the Alpine tectonic reactivation is commonly referred to as 'Hercynian Corsica', since it consists of

Carboniferous to Permian intrusives and volcanics (e.g. Paquette et al., 2003 and Tribuzio et al., 2009). A North–South trending deformation zone, labeled Central Corsica Fault Zone (Maluski et al., 1973 and Waters, 1990), with predominantly strike-slip kinematics separates Hercynian Corsica from 'Alpine Corsica', characterized by variable extents of Alpine deformation and metamorphism (Vitale Brovarone et al., 2013). Basement–cover relationships and comparisons with the Western Alps result in Jurassic paleogeographic reconstructions where the proximal European margin, represented by Hercynian Corsica, graded outboard into a transitional domain, now sampled in the Corte slices, Caporalino unit and Santa Lucia nappe, followed by an 'oceanic domain' (e.g. Rossi et al., 1994 and Rossi et al., 2006 and references therein). The latter mostly consisted of serpentinized lithospheric mantle overlain by pillow lavas, Middle-Upper Jurassic cherts and, locally, slivers of allochthonous continental basement (Vitale Brovarone et al., 2011 and Vitale Brovarone et al., 2013).

2.1. The Santa Lucia nappe

The Santa Lucia nappe (Fig. 2) is bounded to the west by the Corte slices, to the north by the Caporalino unit (Puccinelli et al., 2012) and to the east and south by the Inzecca unit, which originated from the lithosphere flooring the Jurassic Tethys (Amaudric Du Chaffaut et al., 1972). The Santa Lucia nappe consists of Paleozoic continental basement and Mesozoic sediments. Several sub-units, bounded by steep NS-trending tectonic contacts, may be recognized. In this study, the different sub-units will be referred to as:

(1) the Granitic Complex, mainly consisting of Hbl- to Bt-bearing tonalites and of two-mica microgranitoids (Zibra, 2006);

(2) the Belli Piani unit, which consists of Permian meta-gabbros to meta-gabbro-norites belonging to the Mafic Complex and of Permian diorites, tonalites and granites of the Diorite–Granite Complex (Paquette et al., 2003, Rossi et al., 2006, Zibra et al., 2010 and Zibra et al., 2012). This unit is separated from the Granitic Complex to the west by the Bocca di Civenti Shear Zone, while the eastern margin is marked by the high-angle Mandriola and Tomboni faults (Fig. 2);

(3) the Murato unit, consisting of meta-gabbro-norites from the Mafic Complex and Mesozoic sediments;

(4) the Tralonca unit, consisting of Mesozoic to Tertiary sediments (Tomboni conglomerate and Tralonca Flysch).

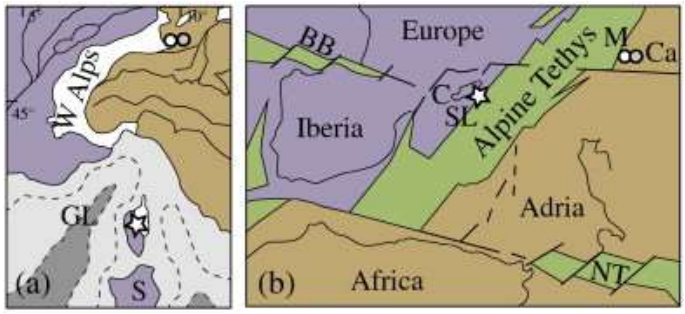

Fig. 1.

(a) Tectonic sketch map of the NW Mediterranean area. Star marks the location of the Santa Lucia nappe (SL). White and gray circles indicate the location of the Malenco Unit (M) and Campo-Grosina units (Ca), respectively. (b) Paleogeographic reconstruction of the Western Tethys in the Early Cretaceous. GL = Gulf of Lion; S = Sardinia; C = Corsica; NT = Neo-Tethys; BB = Bay of Biscay.

Modified from Mohn et al. (2012).

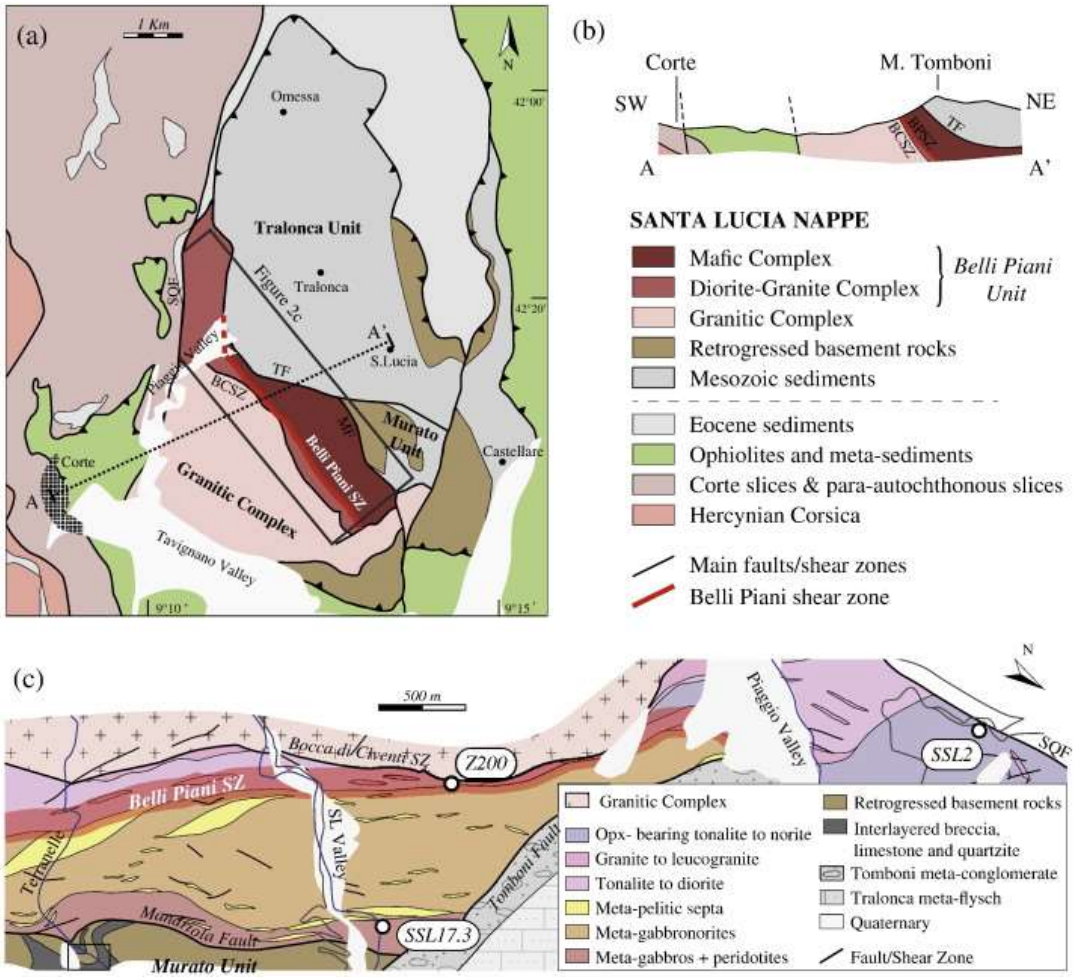

Fig. 2. (a) Tectonic sketch map and (b) representative cross section of the Santa Lucia nappe and surrounding units. BCSZ = Bocca di Civenti Shear Zone; BPSZ = Belli Piani Shear Zone; MF = Murato Fault; SGF = San Quilico Fault; TF = Tomboni Fault. (c) Simplified tectonic map of the Belli Piani Unit. Locations of samples analyzed by $^{40}Ar/^{39}Ar$ geochronology are indicated. Modified after Zibra et al., 2010 and Zibra et al., 2012.

The Granitic Complex and the Belli Piani unit, which are exposed in the western part of the Santa Lucia nappe, experienced minor Alpine deformation and metamorphism, restricted to low-grade metamorphic veins and localized faulting. The Murato and Tralonca units, located in the eastern part, underwent a greater amount of Alpine overprint, resulting in large scale folding and thrusting at T ~ 300 °C (Vitale Brovarone et al., 2013 and Zibra, 2006).

This study is mainly focused on the Mafic Complex and the Diorite–Granite Complex of the Belli Piani unit, where the low extent of Alpine overprint allows detailed investigation of the pre-Alpine tectonometamorphic evolution. The Mafic Complex, which corresponds to the 'Mafic Layered Intrusion' of Libourel (1985), consists of a 2–4 km thick sequence mostly made up of meta-gabbro-norites and minor meta-hornblendites, containing meta-pelitic septa (Fig. 2; Libourel, 1985 and Libourel, 1988). The base of the mafic sequence hosts slices of mantle rocks, reaching up to 50 m in thickness. Magmatic and sub-magmatic fabrics in the Mafic Complex were extensively overprinted by post-intrusion solid state deformation. Pervasive shear fabrics developed during multi-stage deformation under granulite facies conditions, with an early phase at T = 850 ± 50 °C and P = 0.7 ± 0.1 GPa followed by a second step at P ~ 0.5 GPa and T ~ 800 °C (Zibra et al., 2010). High-resolution U–Pb geochronology on zircons separated from meta-pelitic septa yielded three age clusters at ~ 280 Ma, 240 Ma and 190–160 Ma (Rossi et al., 2006). The oldest peak was interpreted to date the granulite facies metamorphism induced by the mafic intrusion (Rossi et al., 2006). Sm–Nd analyses on a metapelite yielded a plagioclase–garnet–whole rock isochron age of 195 ± 9 Ma, interpreted as indicating the onset of cooling of the Mafic Complex at T < 750–800 °C (Rossi et al., 2006).

The Diorite–Granite Complex consists of a magmatic suite of gabbro-dioritic to granitic composition. In the northernmost part of the study area, coarse-grained Opx-bearing tonalites grade westward into an amphibole-rich unit characterized by a millimeter- to meter-scale diorite–tonalite layering (Fig. 2; Zibra et al., 2012). The tonalite–diorite is intruded by a coarse-grained porphyritic granite and then by leucogranite dykes. Magmatic foliation and lineation, defined by euhedral feldspar and amphibole pseudo-phenocrysts, are crosscut by late stage pegmatites and aplites, thereby indicating that the foliation developed before complete solidification of the pluton. The diorite intrusion was emplaced at P ~ 0.5–0.6 GPa (Zibra et al., 2012) at ca. 280 Ma (U–Pb on zircon; Paquette et al., 2003). The magmatic foliation is deformed by a network of anastomosing, high-temperature ductile shear zones, ranging from a few cm to a few m in thickness (Zibra, 2006). These shear zones may be traced for a few tens of meters along strike and exhibit sharp to diffuse boundaries against wall rocks (Zibra et al., 2012).

Sub-magmatic and granulite facies shear fabrics of the Mafic Complex and Diorite–Granite Complex, which have been attributed to Permian deformation (Zibra et al., 2010 and Zibra et al., 2012), are locally overprinted by narrow shear zones developed at amphibolite facies conditions (Zibra, 2006). Medium temperature shearing is especially well preserved at the transition between the Mafic Complex and the Diorite–Granite Complex. Syn-kinematic quartz deformation mechanisms (Zibra et al., 2012) and mineral assemblages (see below) indicate that within this mylonitic belt shearing was accommodated at metamorphic conditions ranging from amphibolite to greenschist facies. Meta-tonalites are characterized by a NW–SE subvertical mylonitic foliation, with a SE plunging stretching lineation marked by quartz ribbons and elongated trails of feldspars, hornblende and biotite. Previous studies (Zibra et al., 2010 and Zibra et al., 2012) suggested that this amphibolite to greenschist facies deformation was related to the late evolution of the Lower Permian deformation event. In this work, newly acquired $^{40}Ar/^{39}Ar$ step heating spectra document that shearing took place in the Jurassic (see below). Therefore, the amphibolite to greenschist facies shear belt will be referred to as Belli Piani shear zone hereafter. Along the Santa Lucia valley, the Belli Piani shear zone grades westward into the younger Bocca di Civenti Shear Zone, characterized

by greenschist facies shear fabrics. In the rest of the area, the Belli Piani shear zone is bounded to the west by tonalites and diorites of the Diorite–Granite Complex, which largely preserve their original sub-magmatic fabrics.

The post-metamorphic evolution of the Santa Lucia basement is characterized by the intrusion of rare, undeformed doleritic dykes (Caby and Jacob, 2000 and Zibra, 2006) and by Mesozoic exhumation to the seafloor (Caby and Jacob, 2000, Libourel, 1985 and Rieuf, 1980). Exposure at the bottom of the Alpine Tethys was suggested based on the presence of clasts derived from the Mafic Complex in the Tomboni meta-conglomerate, which is juxtaposed to the Mafic Complex along the NE part of the study area (Fig. 2c; Caby and Jacob, 2000, Libourel, 1985 and Rieuf, 1980). This polymictic meta-conglomerate contains clasts of granitoids, micaschists, rhyolites, gray limestone and rare serpentinites (Caby and Jacob, 2000) and grades upward into the Tralonca Flysch, whose upper section has been dated to the Cenomanian–Turonian (Rieuf, 1980).

3. Basement exhumation at the basin floor

New unambiguous pre-Alpine relationships between basement rocks and sedimentary cover have been detected in the south-eastern part of the area, in the Murato unit (Fig. 2 and Fig. 3; Zibra, 2006). Despite Alpine deformation, spectacular exposures of basement–cover relationships are widely preserved along the limbs of tight folds in the Mandriola-Punta di Chilgo area. In this domain basement rocks largely consist of meta-gabbro-norites analogous to those of the Belli Piani unit, pervasively re-equilibrated under low-greenschist facies conditions. Towards the contact with the sedimentary cover, meta-gabbro-norites are progressively affected by cataclastic deformation and grade upward into a monogenic fault breccia, consisting of angular clasts ranging in size from a few cm to few dm (Fig. 3a). This 1 to 10 m thick breccia is locally injected by quartz veins. In a few outcrops, the fault breccia is directly overlain by a dark, 1–5 cm thick layered sandstone, consisting of angular fragments from the same crystalline basement (Fig. 3a). Dm-sized clasts of meta-gabbro-norites with high temperature mineral fabrics are locally found within the dark sandstone. Importantly, the quartz-rich matrix of this dark sandstone is almost completely undeformed. These observations indicate that the pervasive low-temperature (mainly brittle) deformation recorded by the metagabbro-derived breccia predates the deposition of the sedimentary cover. The dark sandstone is followed upward by massive limestone strata, enriched in mm- to cm-sized angular clasts of quartz and feldspars, alternating with quartzitic layers and ~ 1 m-thick lenses of breccias and conglomerates (Fig. 3c, d). Lithological layering within the dark sandstone and in the immediately overlying cover is sub-parallel to the basement–cover interface at the scale of several tens of meters. This feature is taken to indicate that sediments onlapped a sub-horizontal top-basement surface.

These new observations allow concluding that the Mafic Complex of the Santa Lucia nappe was exhumed at the floor of the Tethys basin. Final exhumation to the basin floor was achieved through the activity of brittle faults, as indicated by widespread evidence of cataclastic deformation along the top-basement surface. Furthermore, the parallel attitude of sedimentary bedding in the dark sandstone with respect to the top-basement surface suggests that basement exhumation was achieved at the footwall of a low-angle detachment fault.

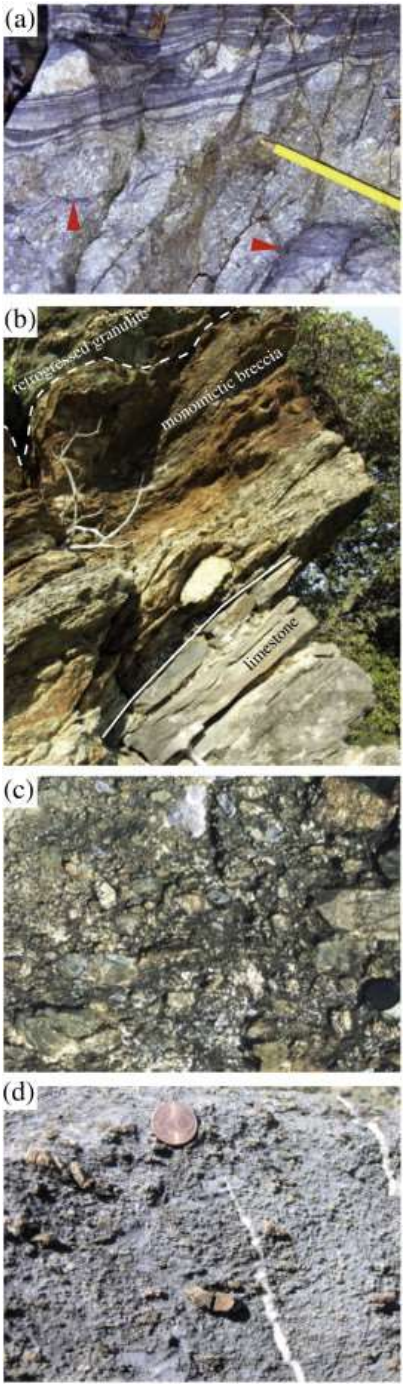

Fig. 3.

Evidence of exhumation of the Mafic Complex in the Murato unit at the bottom of the Alpine Tethys. (a) Preserved stratigraphic contact between layered sandstone and the underlying fault breccia developed at the expense of the meta-gabbronorite (Terranelle Valley). Sandstone contains angular clasts of anorthosite. Red arrowheads point to pre-Alpine cataclasites, which do not propagate through the sediments. (b) Overturned contact between actinolite–chlorite schists, developed at the expense of former granulites, grading into a monogenic meta-breccia with clasts of mafic granulites (Castellare di Mercurio area). The latter are underlain by limestone with clasts of continental basement. In the same location where picture (a) was taken, a polymictic sedimentary breccia is found a few meters from the top-basement surface (c), interlayered with gray limestone with clasts of continental basement (d).

4. Petrography of samples selected for $^{40}Ar/^{39}Ar$ geochronology

4.1. Sample description

Three samples were selected for $^{40}Ar/^{39}Ar$ geochronology on amphibole by the step heating technique, in order to constrain the timing of the tectonometamorphic evolution of the Mafic Complex and Diorite–Granite Complex. The samples were collected in the Belli Piani unit (see Fig. 2 for sample location).

SSL17.3 is a meta-hornblendite from the easternmost part of the Mafic Complex (Fig. 2). In this domain, the compositional layering is isoclinally folded and the shape preferred orientation of large amphibole crystals (Amph I) and rare biotites define a planar anisotropy parallel to the fold axial planes. Brown amphibole crystals display a seriated size distribution (Fig. 4a), with (1) rare subhedral large crystals (> 1 mm; Amph I), with apatite and zircon inclusions, (2) common medium-sized crystals (~ 200–600 μm; Amph II) with sharp grain boundaries and frequent triple junctions, giving rise to a granoblastic texture, in amphibole-dominated domains (Fig. 4b) and (3) finer grained crystals in rare gabbroic pods (Amph III). Rare plagioclase, characterized by a globular shape, is also restricted to the gabbroic pods. Equigranular clinopyroxene crystals, with equant shape and straight grain boundaries, are heterogeneously distributed within the meta-hornblendite selected for this study. In amphibole-rich domains, globular clinopyroxene is generally located along the grain boundaries of adjacent larger amphibole crystals. In gabbroic pods, instead, pyroxene crystals display larger grain size and granoblastic textures, with amphibole as interstitial phase. Minor re-equilibration of the minerals described so far is restricted to the selvages of veinlets consisting of green amphibole (Amph IV) + epidote + titanite that dissect the high-T mineralogy. Furthermore, chlorite replacing pre-existing biotite is commonly observed.

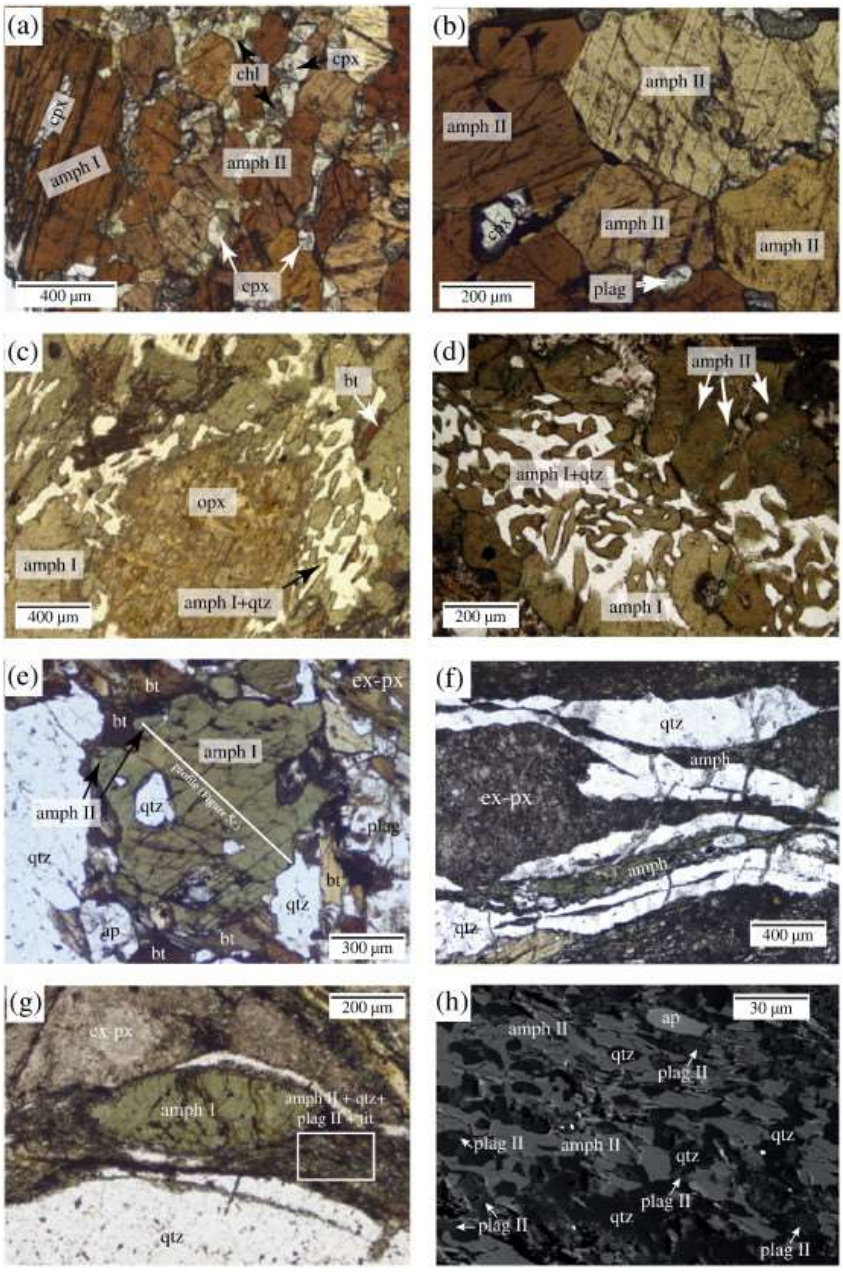

Fig. 4.

Photomicrographs of the samples selected for $^{40}Ar/^{39}Ar$ geochronology and of other representative specimens. Sample SSL17.3 (a, b), collected in the Mafic Complex, is a meta-hornblendite with rare, large porphyroclastic brown amphibole (amph I) and abundant granoblastic amphibole II. Plagioclase and clinopyroxene, locally retrogressed to chlorite (a), are found as interstitial phases. Opx-bearing tonalites from the Diorite–Granite Complex (c, d, e) preserve relict orthopyroxene (c, sample SSL22), replaced by amphibole I + quartz symplectites. Amphibole I is zoned, with green-brown rims (d, sample SSL22 and e, sample SSL2). The white line across a large amphibole crystal (e) indicates the compositional profile shown in Fig. 5c. The Belli Piani shear zone is shown in f, g and h. Along this mylonitic belt, px-bearing tonalites are pervasively deformed, with asymmetric strain fringes developing around former pyroxenes (f, sample V34), plagioclase I and zoned amphibole porphyroclasts. Strain fringes locally contain the assemblage amphibole II + plagioclase II + quartz + apatite + titanite + biotite (g, h, sample Z200).

SSL2 is an Opx-bearing tonalite collected from the northern part of the Diorite–Granite Complex (Fig. 2a). This domain is characterized by the frequent preservation of the original magmatic and sub-magmatic fabrics, with primary orthopyroxene partially replaced by brown-green amphibole (amphibole I) + quartz symplectites or biotite + quartz aggregates (Fig. 4c; Zibra et al., 2012). SSL2 displays a weak magmatic foliation, mainly defined by the alignment of biotite and plagioclase (An = 36 mol%). Biotite + quartz aggregates developed at the expense of orthopyroxene are rare. Green-brown amphibole (Amph I), rich in apatite and zircon inclusions, is generally found associated with quartz around orthopyroxene, or in contact with biotite crystals. As commonly observed in similar lithologies in the area, Amph I crystals are generally zoned, with a second generation of dark green amphibole (Amph II) located both along the rims and along the cleavage planes of Amph I (Fig. 4d, e). Low grade re-equilibration is rare: no chloritization of the original biotite is observed and plagioclase of igneous origin is preserved.

In the central and southern part of the Belli Piani unit, tonalites of the Diorite–Granite Complex similar to SSL2 are variably deformed and recrystallized in the Belli Piani Shear Zone. Sample Z200, which was selected for $^{40}Ar/^{39}Ar$ geochronology, is a mylonitic leucotonalite characterized by sub-cm sized plagioclase porphyroclast and mm-sized green-brownish Amph I porphyroclasts. The latter are commonly zoned, with a homogenous core and a thin rim of dark green amphibole, which is also locally observed along cleavage planes. The original mineral assemblage, consisting of biotite I + plagioclase I + amphibole I + quartz + apatite + zircon is wrapped around by a pervasive fabric formed during non-coaxial flow, as indicated by asymmetric strain fringes around amphibole and plagioclase porphyroclasts (Fig. 4f, g). Ductile shearing was characterized by sinistral sense of shear in present day coordinates. Strain fringes consist of fine grained aggregates (diameter ~ 10 μm) of a second generation of green amphibole (Amph II), associated with plagioclase II (Pl II), quartz and minor titanite, biotite II and apatite (Fig. 4h). Deformation also resulted in the formation of subgrains around Amph I porphyroclasts. Later re-equilibration under static conditions led to the extensive replacement of original plagioclase by fine-grained aggregates of white mica ± albite and to the common chloritization of original biotite. Amphibole retrogression is restricted to rare chlorite veins dissecting amphibole porphyroclasts.

4.2. Mineral chemistry

Amphibole mineral chemistry of the dated samples was determined with a JEOL JXA-8200 electron microprobe located at Dipartimento di Scienze della Terra, Università degli Studi di Milano (Italy); conditions of analyses were 15 kV and 5 nA, and natural standards were employed. The amphibole nomenclature is after Leake et al. (1997).

The brown amphiboles distinguished on microstructural ground in the meta-hornblendite (SSL17.3) are characterized by homogeneous compositions, falling in the Ti-pargasite field (Table 1). The rare green amphibole found in the veins yielded actinolitic compositions. Ti-pargasite has constant Ca/K ratios in the 5.7–6.1 range, while actinolitic amphibole is characterized by very low K content and Ca/K > 60 (generally in the 138–171 range; Fig. 5a).

Sub-unit	Belli Piani SZ	Belli Piani SZ	Belli Piani SZ	Belli Piani SZ	Belli Piani SZ	*Belli Piani SZ*	*Belli Piani SZ*	Diorite-Granite Complex	Diorite-Granite Complex	Diorite-Granite Complex	Diorite-Granite Complex	Diorite-Granite Complex	Diorite-Granite Complex	Diorite-Granite Complex	Diorite-Granite Complex	Mafic Complex	Mafic Complex	Mafic Complex	Mafic Complex	Belli Piani SZ	*Belli Piani SZ*	
Sample	Z200	Z200	Z200	Z200	Z200	*Z200*	*Z200*	SL2	SL2	SL2	SL2	SL2	SL2	SL2	SL2	SL17.3	SL17.3	SL17.3	SL17.3	Z200	*Z200*	
Thin section site	A3	A1	A3	A3	A1	*A3*	*A3*	A1	A2	A2	A3	A1	A1	A2	A2	A2	A2	A2	A2	A2	*A3*	
Mineral	amph I core Tsch	amph I core Prg	amph I core Prg	amph I rim Mg-hbl	amph I rim Mg-hbl	*amph II Mg-hbl*	*amph II Mg-hbl*	amph I Fe-hbl	amph I Fe-prg	amph I Fe-prg	amph I Fe-prg	amph II Fe-prg	amph II Fe-prg	amph II Fe-prg	amph II Fe-prg	amph I Prg	amph I Prg	amph IV Act	amph IV Act	plag II	*plag II*	
SiO_2	42.33	42.91	42.36	43.95	45.77	*46.89*	*46.15*	44.11	41.35	41.08	41.06	40.91	40.89	42.05	40.99	41.13	40.87	53.22	52.25	57.13	*56.78*	
TiO_2	1.65	1.40	1.62	1.54	1.40	*1.10*	*1.39*	1.59	2.08	2.16	2.13	1.65	1.06	1.26	1.49	4.17	4.13	0.11	0.13	0.03	*0.00*	
$Al2O_3$	11.37	11.74	11.39	9.66	9.31	*7.78*	*8.61*	9.96	11.73	11.62	11.60	12.82	12.81	11.60	12.34	13.36	13.44	2.59	3.98	27.43	*27.62*	
Cr	0.03	0.00	0.02	0.01	0.00	*0.00*	*0.06*	0.00	0.01	0.00	0.00	0.02	0.00	0.01	0.08	0.12	0.14	0.00	0.00	0.00	*0.00*	
FeO	17.14	16.81	17.35	16.50	15.89	*16.05*	*15.76*	20.36	21.26	20.76	21.31	20.07	21.19	20.65	20.73	14.05	13.99	13.27	15.63	0.48	*0.47*	
MnO	0.27	0.44	0.37	0.36	0.41	*0.49*	*0.46*	0.37	0.34	0.27	0.31	0.25	0.27	0.24	0.28	0.14	0.17	0.26	0.27	0.00	*0.00*	
MgO	10.36	11.00	10.58	11.26	12.30	*12.26*	*12.22*	8.40	7.81	7.67	7.53	7.80	7.67	8.54	7.72	11.08	11.00	15.66	13.62	0.02	*0.02*	
CaO	11.21	11.17	11.16	11.49	11.18	*11.35*	*11.52*	11.50	11.01	10.89	10.99	11.38	11.51	11.36	11.50	11.27	11.42	12.37	12.05	9.33	*9.57*	
Na_2O	1.26	1.57	1.43	1.11	1.32	*1.01*	*1.05*	1.18	1.48	1.41	1.32	1.33	1.12	1.18	1.17	2.17	2.07	0.38	0.46	5.93	*5.88*	
K_2O	1.47	1.24	1.42	1.17	0.88	*0.73*	*0.94*	1.39	1.71	1.72	1.69	1.84	2.08	1.71	1.88	1.65	1.61	0.06	0.06	0.27	*0.24*	
Cl	0.14	0.04	0.10	0.10	0.07	*0.05*	*0.08*	0.14	0.19	0.20	0.16	0.25	0.33	0.25	0.23	0.03	0.01	0.05	0.08	0.00	*0.00*	
Total	97.23	98.32	97.80	97.14	98.52	*97.81*	*98.23*	99.01	98.96	97.78	98.09	98.31	98.93	98.85	98.41	99.17	98.85	97.98	98.55	100.62	*100.58*	
Si	6.34	6.32	6.31	6.55	6.67	*6.88*	*6.75*	6.60	6.24	6.27	6.25	6.20	6.17	6.29	6.21	6.03	6.01	7.63	7.54	2.55	*2.54*	
Ti	0.19	0.15	0.18	0.17	0.15	*0.12*	*0.15*	0.18	0.24	0.25	0.24	0.19	0.12	0.14	0.17	0.46	0.46	0.01	0.01	0.00	*0.00*	
Al	2.01	2.04	2.00	1.70	1.60	*1.34*	*1.48*	1.76	2.09	2.09	2.08	2.29	2.28	2.07	2.20	2.31	2.33	0.44	0.68	1.44	*1.46*	
Cr	0.00	0.00	0.00	0.00	0.00	*0.00*	*0.01*	0.00	0.00	0.00	0.00	0.00	0.00	0.00	0.01	0.01	0.02	0.00	0.00	0.00	*0.00*	
Fe^{2+}	1.55	1.39	1.49	1.46	1.34	*1.45*	*1.41*	2.18	2.15	2.17	2.18	2.09	2.02	1.93	2.07	1.45	1.46	1.32	1.67	0.00	*0.00*	
Fe^{3+}	0.60	0.69	0.68	0.60	0.60	*0.52*	*0.52*	0.37	0.54	0.48	0.53	0.46	0.66	0.68	0.56	0.27	0.27	0.27	0.21	0.00	*0.00*	
Mn	0.03	0.05	0.05	0.05	0.05	*0.06*	*0.06*	0.05	0.04	0.03	0.04	0.03	0.03	0.04	0.04	0.02	0.02	0.03	0.03	0.00	*0.00*	
Mg	2.31	2.42	2.35	2.50	2.67	*2.70*	*2.67*	1.87	1.76	1.75	1.71	1.76	1.73	1.87	1.74	2.42	2.41	3.35	2.93	0.00	*0.00*	
Ca	1.80	1.76	1.78	1.83	1.74	*1.78*	*1.81*	1.84	1.78	1.78	1.79	1.85	1.86	1.85	1.87	1.77	1.80	1.90	1.86	0.45	*0.46*	
Na	0.37	0.45	0.41	0.32	0.37	*0.29*	*0.30*	0.34	0.43	0.42	0.39	0.39	0.33	0.33	0.34	0.62	0.59	0.11	0.13	0.51	*0.51*	
K	0.28	0.23	0.27	0.22	0.16	*0.14*	*0.17*	0.27	0.33	0.33	0.33	0.36	0.40	0.34	0.36	0.31	0.30	0.01	0.01	0.02	*0.01*	
Fe	2.15	2.07	2.16	2.06	1.94	*1.97*	*1.93*	2.55	2.69	2.65	2.72	2.55	2.68	2.61	2.63	1.72	1.72	1.59	1.89	0.02	*0.02*	
Cl	0.02	0.01	0.02	0.02	0.01	*0.01*	*0.01*	0.03	0.03	0.04	0.03	0.04	0.06	0.06	0.04	0.00	0.00	0.01	0.01	0.00	*0.00*	
cation sum	15.49	15.50	15.51	15.40	15.35	*15.28*	*15.32*	15.46	15.59	15.57	15.55	15.61	15.60	15.53	15.58	15.67	15.70	15.06	15.08	4.99	*4.99*	
Fe^{3+}/Fetot	0.28	0.33	0.31	0.29	0.31	*0.26*	*0.27*	0.15	0.20	0.18	0.20	0.18	0.25	0.26	0.21	0.16	0.15	0.17	0.11	0.46	*0.47*	XCa
Al (4)	1.66	1.68	1.69	1.45	1.33	*1.12*	*1.25*	1.40	1.76	1.73	1.75	1.80	1.83	1.71	1.79	1.97	1.99	0.37	0.46	0.53	*0.52*	XNa
Al (8)	0.35	0.36	0.31	0.25	0.26	*0.22*	*0.24*	0.36	0.33	0.36	0.33	0.49	0.45	0.35	0.42	0.34	0.34	0.07	0.21			
Na (M4)	0.16	0.18	0.17	0.14	0.18	*0.14*	*0.15*	0.15	0.17	0.18	0.16	0.13	0.13	0.13	0.12	0.25	0.22	0.05	0.06			
Na (A)	0.21	0.27	0.24	0.18	0.19	*0.14*	*0.15*	0.19	0.26	0.24	0.23	0.26	0.20	0.20	0.22	0.36	0.37	0.05	0.07			
Mg/(Mg + Fe)	0.52	0.54	0.52	0.55	0.58	*0.58*	*0.58*	0.42	0.40	0.40	0.39	0.41	0.39	0.42	0.40	0.58	0.58	0.68	0.61			
Na (A) + K	0.49	0.50	0.51	0.40	0.35	*0.28*	*0.32*	0.46	0.59	0.57	0.55	0.61	0.60	0.53	0.58	0.67	0.67	0.06	0.08			
Ca/K	6.40	7.57	6.60	8.25	10.70	*13.01*	*10.33*	6.95	5.41	5.32	5.46	5.19	4.65	5.58	5.14	5.74	5.96	171.16	156.42			
Cl/K	0.09	0.03	0.06	0.08	0.07	*0.06*	*0.08*	0.09	0.10	0.11	0.09	0.12	0.15	0.13	0.11	0.02	0.01	0.79	1.19			
max P						*0.5–0.6*	*0.5–0.6*															
T (°C; Holland & Blundy, 1994)						*701–709*	*715–723*															

Table 1.

Representative compositions of amphibole and plagioclase. Gray background indicates amphibole and plagioclase compositions used to estimate the temperature of shearing along the Belli Piani shear zone. Amphibole normalization follows Holland and Blundy, 1994.

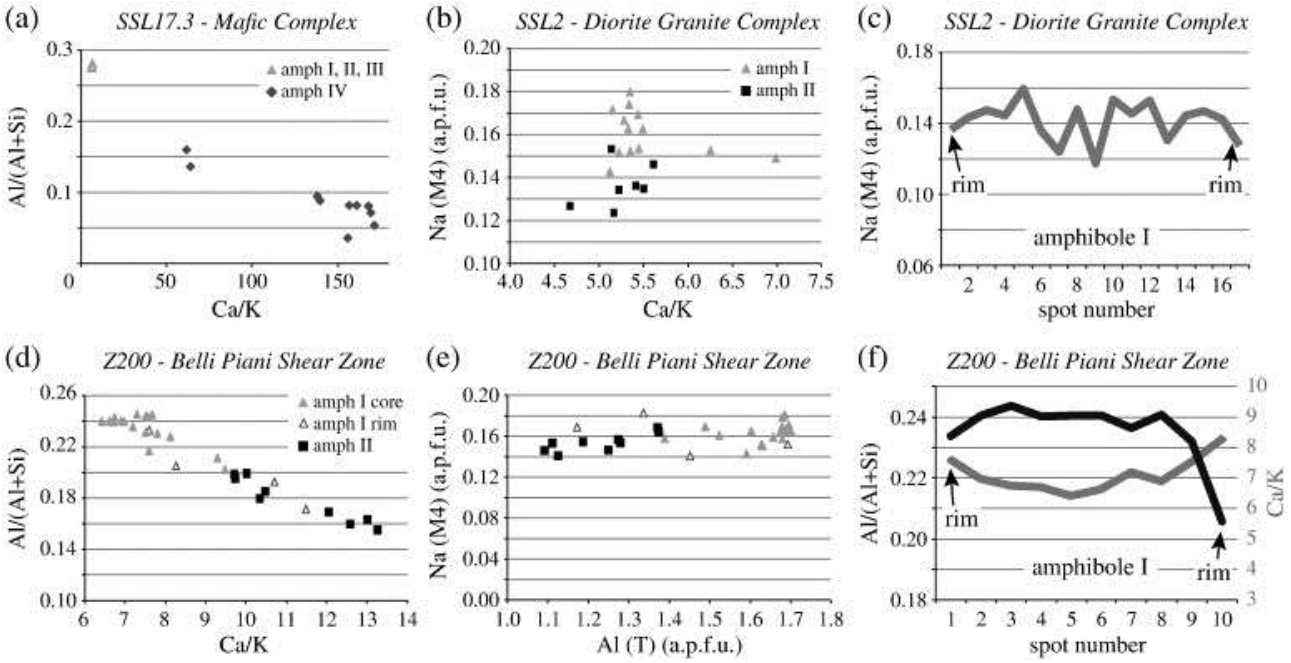

Fig. 5.

Compositional range of the different amphibole generations defined on microstructural ground. (a) Al/(Al + Si) vs. Ca/K plot for the horneblendite SSL17.3 (note that 10 mineral compositions have been plotted with gray triangles); Na(M4) vs. Ca/K plot (b) and Ca/K compositional profile (c) for amphiboles from the opx-bearing tonalite SSL2; Al/(Al + Si) vs. Ca/K plot (d), Na(M4) vs. Al(T) plot (e) and Ca/K and Al/(Al + Si) (f) compositional profiles for amphiboles from the mylonitic leucotonalite Z200.

Analyses carried out on the opx-bearing tonalite (SSL2) revealed a slight compositional difference between the brown-green amphibole cores (Amph I), which display a Fe-hornblende to Fe-pargasite composition, and the dark green rims, which yielded a Fe-pargasite composition (Table 1). Amph I is characterized by a higher Na content in the M4 site with respect to Amph II (0.15–0.17 a.p.f.u. vs 0.12–0.13 a.p.f.u.). Ca/K ratios estimated from analyses performed on the two different amphibole generations as identified on petrographic and microstructural ground largely overlap. This overlap is attributed to the patchy re-equilibration visible under the microscope, which is also evident from the compositional profile shown in Fig. 5c. However, a few analyses yielded lower Ca/K ratios of ca. 4.5 for Amph II and values as high as 7 for Amph I (Table 1). These values are considered as the best approximation of the actual Ca/K ratios of the two amphibole end members.

The two amphibole generations detected on microstructural ground in Z200 are characterized by marked compositional differences. Amph I porphyroclasts are compositionally zoned, with tschermakitic to pargasitic cores, while Mg-hornblende compositions are characteristic both of the rims (Fig. 5d, f) and of the syn-kinematic amphibole in the strain shadows. Amph I cores and rims yielded Ca/K = 6.0–7.5 and 8–10, respectively. Amph II displays a relatively wide range of compositions, with Ca/K = 10–20 and Al/(Al + Si) = 0.11–0.18, depending on the presence/absence of Pl II. When closely associated with Pl II (Fig. 4h), Amph II compositions are relatively constant, with Ca/K = 10–13 and Al/(Al + Si) = 0.16–0.18. Note that the composition of the rims of amphibole porphyroclasts converge towards that of amphibole II. The Na content in the M4 site is characterized by a minor decrease from the 0.16 – 0.18 a.p.f.u. estimated for the porphyroclasts' cores to the values of 0.14–0.15 a.p.f.u. characteristic of the syn-kinematic amphibole (Fig. 5e). Pl II is characterized by andesine composition (An = 46.5–47.5 mol%; Table 1).

5. $^{40}Ar/^{39}Ar$ step-heating on amphibole

5.1. Analytical techniques

Amphiboles were separated with standard mineral separation techniques and the crystals selected for irradiation were hand-picked from the > 200 μm split. Samples were analyzed by the $^{40}Ar/^{39}Ar$ method at the University of Nevada Las Vegas, where they were wrapped in Al foil and stacked in 6 mm inside diameter Pyrex tubes. Individual packets averaged 3 mm thick and neutron fluence monitors (FC-2, Fish Canyon Tuff sanidine) were placed every 5–10 mm along the tube. Synthetic K-glass and optical grade CaF_2 were included in the irradiation packages to monitor neutron induced argon interferences from K and Ca. Loaded tubes were packed in an Al container for irradiation. Samples irradiated at the Nuclear Science Center at Texas AM University were in-core for 14 h in the D3 position on the core edge (fuel rods on three sides, moderator on the fourth side) of the 1 MW TRIGA type reactor. Irradiations are performed in a dry tube device, shielded against thermal neutrons by a 5 mm thick jacket of B_4C powder, which rotates about its axis at a rate of 0.7 revolutions per minute to mitigate horizontal flux gradients. Correction factors for interfering neutron reactions on K and Ca were determined by repeated analysis of K-glass and CaF_2 fragments. Measured $(^{40}Ar/^{39}Ar)_K$ values were 0.00 (± 0.0002). Ca correction factors were $(^{36}Ar/^{37}Ar)Ca = 2.67\ (\pm 2.70) \times 10^{-4}$ and $(^{39}Ar/^{37}Ar)Ca = 6.782\ (\pm 1.57) \times 10^{-4}$. J factors were determined by fusion of 3–5 individual crystals of neutron fluence monitors which gave reproducibilities of 0.14% to 0.46% at each standard position. Variation in neutron flux along the 100 mm length of the irradiation tubes was < 4%. An error in J of 0.5% was used in age calculations. No significant neutron flux gradients were present within individual packets of crystals as indicated by the excellent reproducibility of the single crystal flux monitor fusions.

Irradiated crystals together with CaF_2 and K-glass fragments were placed in a Cu sample tray in a high vacuum extraction line and were heated using a 20 W CO_2 laser. Samples analyzed by the

furnace step heating method utilized a double vacuum resistance furnace similar to the Staudacher et al. (1978) design. Heating temperatures are listed in Table 2. Gas was collected for 12 min at each temperature step. Reactive gasses were removed by a single MAP and two GP-50 SAES getters prior to being admitted to a MAP 215-50 mass spectrometer by expansion. The relative volumes of the extraction line and mass spectrometer allow 80% of the gas to be admitted to the mass spectrometer for furnace heating analyses. Peak intensities were measured using a Balzers electron multiplier by peak hopping through 7 cycles; initial peak heights were determined by linear regression to the time of gas admission. Mass spectrometer discrimination and sensitivity was monitored by repeated analysis of atmospheric argon aliquots from an on-line pipette system. Measured $^{40}Ar/^{36}Ar$ ratios were 290.07 ± 0.06% during this work, thus a discrimination correction of 1.01651 (4 AMU) was applied to measured isotope ratios. The sensitivity of the mass spectrometer was ~ 6×10^{-17} mol mV^{-1} with the multiplier operated at a gain of 52 over the Faraday. Line blanks averaged 52.71 mV for mass 40 and 0.19 mV for mass 36 for furnace heating analyses. Discrimination, sensitivity, and blanks were relatively constant over the period of data collection. Computer automated operation of the sample stage, laser, extraction line and mass spectrometer as well as final data reduction and age calculations were done using LabSPEC software written by B. Idleman (Lehigh University). An age of 27.9 Ma (Cebula et al., 1986 and Steven et al., 1967) was used for the Fish Canyon Tuff sanidine flux monitor in calculating ages for samples.

The heating schedules and the measured quantities of the different argon isotopes (in mV) from the three samples that have been the subject of this study are listed in Table 2. Ca/K ratios have been calculated for each step. 'Plateau' ages were calculated for suitable samples (SL17.3). For $^{40}Ar/^{39}Ar$ analyses a plateau segment consists of 3 or more contiguous gas fractions having analytically indistinguishable ages (i.e. all plateau steps overlap in age at ± 2σ analytical error) and comprising a significant portion of the total gas released (> 50%). For each sample $^{39}Ar/^{40}Ar$ vs $^{36}Ar/^{40}Ar$ plots are examined to check for the effects of excess argon. All analytical data are reported at the confidence level of 1σ (standard deviation) and uncertainties for J are included. Uncertainties for decay constant and standard age are not included.

Table 2.

$^{40}Ar/^{39}Ar$ stepwise heating results.

Step	T (°C)	^{36}Ar (mV)	^{37}Ar (mV)	^{38}Ar (mV)	^{39}Ar (mV)	^{40}Ar (mV)	% $^{40}Ar^*$	% ^{39}Ar released	Ca/K	$^{40}Ar^*/^{39}ArK$	Age (Ma)	± 1σ
Z200 amphibole (*weight = 20.35 mg, J = 0.001639 ± 0.5%*)												
1	800	47.55	63.98	9.62	29.93	15502.10	11.70	7.82	6.48	61.14	172.29	4.53
2	900	7.01	34.93	1.70	24.31	2738.32	26.40	6.35	4.36	29.91	86.35	1.06
3	1000	4.21	101.09	1.18	23.79	2777.16	56.80	6.22	12.91	66.93	187.80	1.40
4	1030	1.06	159.60	0.88	44.69	3331.78	91.50	11.68	10.85	68.80	192.75	1.17
5	1050	0.62	140.97	0.73	41.28	2977.48	94.70	10.79	10.37	68.85	192.90	1.19
6	1070	0.54	125.61	0.66	38.26	2790.66	95.10	10.00	9.97	69.92	195.73	1.18
7	1090	0.44	99.95	0.50	29.76	2228.94	95.10	7.77	10.20	71.75	200.59	1.21
8	1115	0.62	111.26	0.56	29.44	2237.27	93.00	7.69	11.48	71.16	199.02	1.22
9	1145	0.73	131.94	0.66	34.70	2712.66	93.10	9.07	11.55	73.34	204.79	1.32
10	1175	0.42	67.04	0.33	16.01	1273.66	91.80	4.18	12.72	73.45	205.08	1.25
11	1200	0.37	61.51	0.30	16.02	1258.06	92.80	4.19	11.66	73.65	205.61	1.25
12	1225	0.46	81.36	0.39	21.26	1636.09	93.00	5.56	11.62	72.03	201.31	1.23
13	1255	0.45	94.92	0.44	23.15	1763.28	93.70	6.05	12.46	71.86	200.87	1.24
14	1400	0.37	90.81	0.23	10.13	821.14	89.80	2.65	27.37	72.67	203.00	1.28
SSL2 amphibole (weight = 22.83 mg, J = 0.0015165 ± 0.5%)												
1	750	31.36	18.38	6.61	35.81	12449.30	26.90	5.70	1.66	93.73	239.76	1.77
2	850	4.86	15.43	1.67	51.77	4909.57	71.70	8.20	0.96	67.94	176.91	0.94
3	950	1.79	30.27	0.85	37.07	3130.57	84.60	5.90	2.65	70.96	184.38	0.92
4	990	0.93	39.75	0.60	28.53	2825.25	91.90	4.50	4.52	90.31	231.56	1.14
5	1010	0.83	82.38	0.86	45.35	4863.79	96.00	7.20	5.89	102.81	261.39	1.27

Step	T (°C)	^{36}Ar (mV)	^{37}Ar (mV)	^{38}Ar (mV)	^{39}Ar (mV)	^{40}Ar (mV)	% ^{40}Ar*	% ^{39}Ar released	Ca/K	^{40}Ar*/^{39}ArK	Age (Ma)	± 1σ
6	1030	0.77	109.35	1.02	58.44	6284.96	97.30	9.30	6.07	104.64	265.71	1.29
7	1050	0.58	106.09	0.97	58.76	6138.07	98.10	9.30	5.85	102.49	260.64	1.33
8	1070	0.55	131.11	1.18	73.59	7575.50	98.60	11.70	5.78	101.65	258.64	1.25
9	1090	0.37	84.34	0.83	52.23	5161.91	98.90	8.30	5.23	97.60	249.03	1.23
10	1110	0.31	46.66	0.53	32.13	3004.04	99.30	5.10	4.71	91.52	234.46	1.18
11	1130	0.33	68.94	0.58	35.02	3606.06	99.40	5.60	6.38	101.22	257.62	1.32
12	1150	0.24	37.27	0.30	16.48	1744.38	100.00	2.60	7.33	102.80	261.36	1.32
13	1180	0.30	56.95	0.43	24.31	2668.80	99.30	3.90	7.60	107.28	271.95	1.31
14	1220	0.46	115.19	0.86	51.19	5677.36	99.00	8.10	7.30	109.29	276.68	1.34
15	1400	0.48	63.56	0.52	28.33	3218.77	99.40	4.50	7.28	109.67	277.57	1.33
SSL17-3 amphibole (weight = 12.23 mg, J = 0.001522 ± 0.5%)												
1	750	9.68	13.15	1.97	3.31	3252.27	13.70	0.90	13.08	135.43	338.11	3.03
2	850	1.46	6.78	0.32	3.00	579.14	28.30	0.80	7.43	52.57	138.87	0.95
3	950	0.75	26.99	0.21	3.94	434.09	56.00	1.10	22.61	57.04	150.19	0.83
4	1000	0.55	18.46	0.14	2.65	339.36	61.00	0.70	22.99	70.28	183.33	1.15
5	1030	0.41	15.73	0.13	4.04	389.38	78.10	1.10	12.82	68.60	179.15	0.96
6	1050	0.34	21.81	0.17	7.47	570.28	89.50	2.00	9.61	64.35	168.56	0.91
7	1065	0.33	50.93	0.32	19.72	1333.82	96.10	5.40	8.49	63.61	166.72	0.84
8	1090	0.48	125.38	0.75	50.34	3284.59	97.40	13.80	8.19	63.20	165.69	0.83
9	1120	0.50	134.93	0.79	54.02	3521.07	98.10	14.80	8.21	63.23	165.75	0.82
10	1160	0.49	116.04	0.64	45.15	2975.68	97.70	12.40	8.45	63.51	166.47	0.84
11	1200	0.44	131.75	0.78	53.38	3452.31	98.60	14.60	8.11	63.04	165.30	0.85
12	1245	0.64	230.10	1.26	88.77	5721.37	98.30	24.30	8.52	63.10	165.45	0.83
13	1400	0.47	91.33	0.49	29.64	1992.12	99.40	8.10	10.14	63.46	166.35	0.86

5.2. Step-heating spectra

Amphiboles from the meta-hornblendite of the Mafic Complex (SSL17.3) yielded a relatively simple apparent age pattern (Fig. 6a). The first 5 steps of the step heating experiment, characterized by a cumulative ^{39}Ar release < 5%, yielded high atmospheric argon content, low $^{40}Ar^{*}$ and erratic Ca/K ratios in the 7.4–23 range. All the other steps (6–13), comprising more than 95% of the total ^{39}Ar released, are characterized by high $^{40}Ar^{*}$ and constant Ca/K ratios in the 8.2–10.1 range. Apparent ages fall consistently in the 165–168 Ma range, and a 'plateau' age of 165.4 ± 1.7 Ma can be calculated for steps 7–13 (93.3% of ^{39}Ar released; MSWD = 0.42). The spread of data in the $^{36}Ar/^{40}Ar$ vs. $^{39}Ar/^{40}Ar$ diagram indicates that the specimen is largely devoid of extraneous argon (Fig. 6b).

Amphiboles from the Opx-bearing tonalite of the Diorite–Granite Complex (SSL2) yielded a double-humped spectrum (Fig. 6c). A first step, characterized by very low $^{40}Ar^{*}$, is followed by a second step yielding an apparent age of 176.9 ± 0.9 Ma. A step-wise increase in apparent ages culminates with estimates of 265.7 ± 1.3 at step 6, followed by a progressive decrease between steps 7 and 10, reaching a relative minimum at 234.5 ± 1.2 Ma. A renewed increase culminates in an apparent age of 277.6 ± 1.3 Ma for the last step (step 15). Inspection of the $^{36}Ar/^{40}Ar$ vs. $^{39}Ar/^{40}Ar$ diagram shows that data points are mostly clustered close to the $^{39}Ar/^{40}Ar$ axis (Fig. 6d). As illustrated in Fig. 6e, there is a correlation between estimated ages and Ca/K ratios calculated for each individual step. More specifically, Ca/K ratios decrease progressively from 7 – 8 for the oldest steps to 1 in the youngest step, with most steps falling in the 4.5–6.5 range.

Amphiboles separated from the mylonitic tonalite of the Diorite–Granite Complex (Z200) yielded a slightly discordant spectrum with a weak convex-upward shape (Fig. 6f). After the first two steps, characterized by low $^{40}Ar^{*}$ and low Ca/K ratios, steps 3 to 11 are characterized by the progressive increase of apparent ages from 187.8 ± 1.4 to 205.6 ± 1.2 Ma. Steps 12–13 yielded slightly younger ages, down to 200.9 ± 1.2, prior to a renewed increase to 203.0 ± 1.3 for the last step. The Ca/K ratios range from 10 to 12.5, excluding the first two steps and the last step, possibly affected by minor biotite and apatite contaminations, with no correlation with the apparent ages (Fig. 6h).

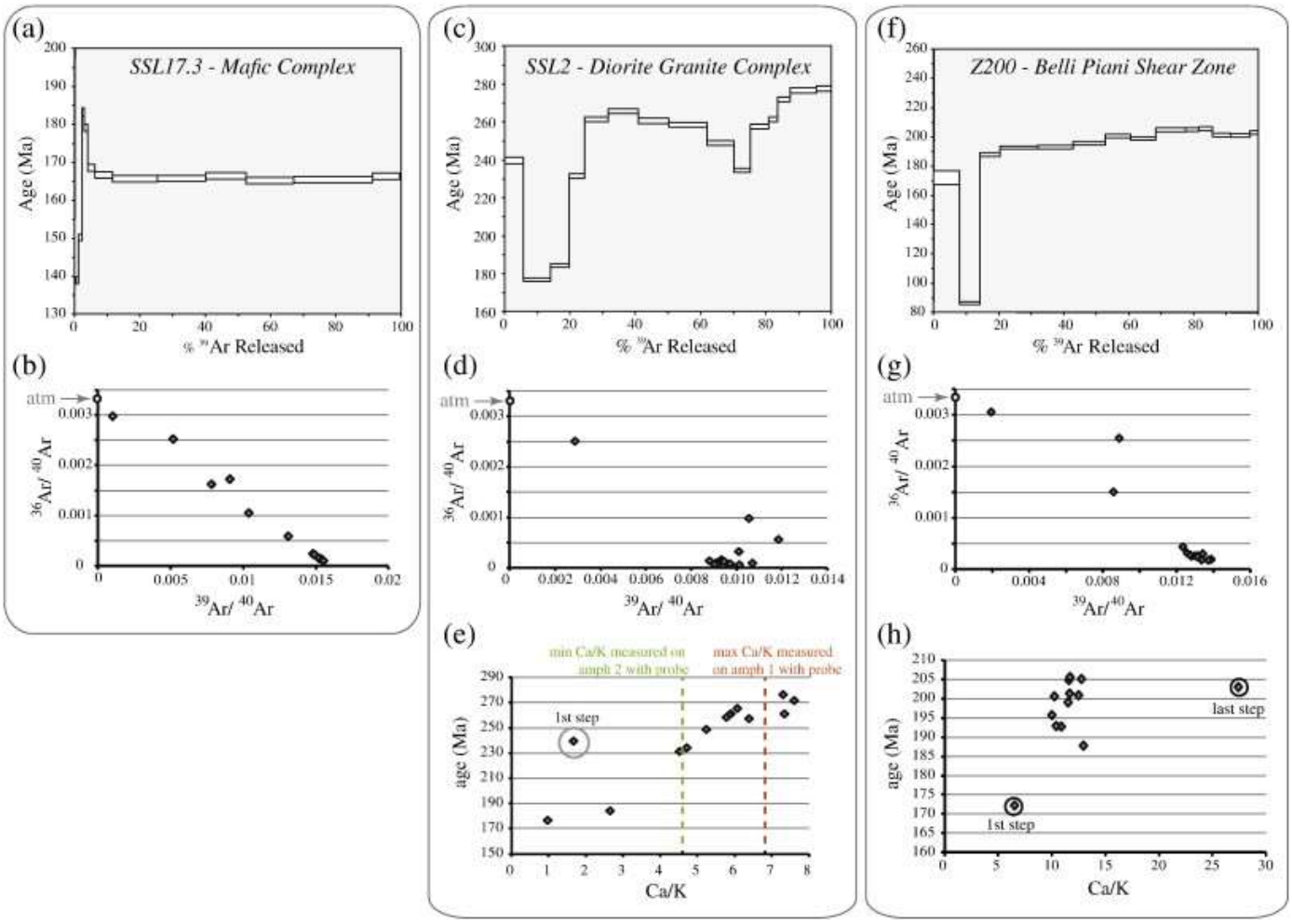

Fig. 6.

$^{40}Ar/^{39}Ar$ step-release spectra (a, c, f), $^{39}Ar/^{40}Ar$ vs $^{36}Ar/^{40}Ar$ plots (b, d, g) and element ratios for individual heating steps (e, h) for analyzed samples. Sample SSL17.3, from the Mafic Complex, yielded a flat apparent age spectrum (a). Sample SSL2 yielded a double-hump spectrum (c). Element correlation diagrams indicate that higher apparent ages are characterized by higher Ca/K (e). No such correlation is apparent for sample Z200 (h), which yielded a slightly convex upward spectrum (f).

6. Discussion

6.1. Interpretation of the step-heating spectra

Assessing the geological significance of $^{40}Ar/^{39}Ar$ spectra hinges on the ability to correlate step-heating experiment data with mineral chemistry and textural information. As most amphibole-bearing rocks commonly contain more than one generation of amphibole, element correlation diagrams provide efficient tools to link the isotopic information from the step-heating experiment to the compositional data from microprobe investigations (e.g. Di Vincenzo and Palmeri, 2001 and Villa et al., 2000). This approach, applied to the spectra yielded by the samples from the Belli Piani unit, provides important insights on the tectonic evolution of this domain from the Permian to the Jurassic.

The meta-hornblendite (SSL17.3) was collected from the eastern part of the Mafic Complex. The Ca/K ratios calculated for each step of the step-heating experiment, which falls in the 8–10 range, is only slightly higher than the values of ca. 6 normally obtained with electron microprobe analyses on Ti-pargasite (Table 1). This slight discrepancy may be attributed to minor contamination by green actinolitic amphibole (Amph IV), with high Ca/K ratios (> 60), which is locally associated with late metamorphic veins or found as thin rims around Ti-pargasite. Such minor contamination is unlikely to generate a noticeable younging of the estimated ages, due to the negligible K content of the potential contaminant (Table 1). The remarkably flat age spectrum, which is characteristic of > 95% of the ^{39}Ar released, indicates that porphyroclastic and granoblastic Ti-pargasites are characterized by identical Ar isotopic composition, despite significant differences in grain size. Porphyroclastic and granoblastic Ti-pargasites were formed at magmatic to granulite facies conditions, typically affecting slowly cooling mafic intrusives (e.g. Jagoutz et al., 2007 and Müntener et al., 2000). Therefore, the ‘plateau’ age of 165.4 ± 1.7 Ma is interpreted as recording the timing of rapid cooling of pre-existing Ti-pargasite at temperatures preventing significant loss of radiogenic argon from the crystal lattice. This temperature normally falls in the 500–600 °C range, depending on grain size, cooling rate and mineral composition (e.g. McDougall and Harrison, 1999).

This evolution is markedly different from the temperature–time history that is inferred for the Opx-bearing tonalite of the Diorite–Granite Complex (SSL2). The $^{40}Ar/^{39}Ar$ spectrum of this sample is characterized by a double hump. Humped spectra from white mica (Beltrando et al., 2009 and Wijbrans and McDougall, 1986) and amphibole (Villa et al., 2000) were repeatedly interpreted to result from mixing of mineral generations with different apparent age and composition. As shown above (Fig. 5b), amphibole I is richer in Ca than amphibole II and older apparent ages are related to a greater contribution of a relatively Ca-rich amphibole (Fig. 6e). Therefore, 277.6 ± 1.3 Ma is interpreted as the minimum age of crystallization of amphibole I. Significantly, this estimate is within error of the youngest available estimate for the intrusion of the Diorite–Granite Complex, at 279.8 ± 1.4 Ma (Paquette et al., 2003). These results indicate that, after rapid cooling following the intrusion, sample SSL2 resided at temperatures too low to allow any significant loss of radiogenic ^{40}Ar from amphibole. As apparent from Fig. 6e, progressively younger apparent ages are associated with decreasing Ca/K, suggesting a greater relative contribution of argon released from Amph II. However, the youngest apparent ages, in the 177–184 Ma range, yielded Ca/K ratios of 0.95 and 2.65, thus lower than the minimum value of Ca/K = 4.65 estimated for Amph II with the electron microprobe (Table 1 and Fig. 5b). This feature hints at the possible presence of a contaminant phase (presumably biotite) in the mineral separate. Considering these limitations, 231.6 ± 1.1 Ma, which yielded Ca/K = 4.5, can tentatively be interpreted as the maximum age of crystallization of Amph II.

Upper Triassic to Jurassic apparent $^{40}Ar/^{39}Ar$ ages are characteristic of the mylonitic tonalite (Z200) collected from the Belli Piani Shear Zone, separating the Mafic Complex from the Diorite–Granite Complex. Due to the small grain size of the syn-kinematic amphibole crystals, the mineral separate for the step-heating experiment consisted exclusively of the zoned amphibole porphyroclasts. Apart for the first 2 steps, characterized by low ^{40}Ar and low Ca/K ratios, possibly related to minor biotite or sericitic white mica contamination, all other steps yielded rather homogeneous Ca/K ratios in the 10.0–12.9 range. These values are intermediate between the Ca/K ratios measured with the electron microprobe in the tschermakitic to pargasitic cores of zoned porphyroclasts (6.4–9.2, with most common values = 7.0–7.5) and in the Mg-hornblende characteristic of the porphyroclast rims and of the strain shadows (Amph I rims = 7.6–10.8; Amph II = 8.2–20.5). This implies that the gas released during the step-heating experiment probably resulted from mixing of the two different reservoirs identified on compositional ground within the porphyroclasts. As a result, 187.8 ± 1.4 Ma is interpreted as the maximum age for crystallization of Mg-hornblende in the Amph I rims and, by extension, of syn-kinematic Mg-hornblende in the strain shadows. The age of 205.6 ± 1.2 Ma, instead, is interpreted as the minimum age of crystallization/cooling of Amph I cores.

6.2. Pressure–temperature evolution of the Belli Piani shear zone

As shown in Section 4, shearing in the Belli Piani shear zone is associated with crystallization of Mg-hornblende + andesine + biotite + quartz ± titanite. The temperature of crystallization of this mineral assemblage may be estimated applying the edenite–tremolite calibration of the amphibole–plagioclase thermometer (Holland and Blundy, 1994). Assuming that the shear fabric formed at P = 0.5–0.6 GPa, which corresponds to the inferred pressure for the intrusion of the magmatic protolith (Zibra et al., 2012), the geothermometer yields T = 700–720 °C. Considering the temperature uncertainty on the applied method (Holland and Blundy, 1994), T = 710 ± 40 °C is proposed for the crystallization of syn-kinematic Mg-hornblende. Assuming lower pressures of re-equilibration would result in slightly higher T estimates.

These temperatures are higher than the estimates of 400–450 °C based on quartz microstructures in the same sample considered here (Zibra et al., 2012). We attribute this discrepancy to late-kinematic strain localization in the Qtz-rich domains. Therefore, we conclude that shearing along the Belli Piani shear zone initiated under amphibolite facies conditions, at T = 710 ± 40 °C, and continued down to greenschist facies conditions.

6.3. Rapid cooling and exhumation of continental basement along a distal margin

The results of the $^{40}Ar/^{39}Ar$ step-heating experiments from the Belli Piani unit and the discovery of the detachment fault in the Murato unit provide unique insights into the progressive thinning recorded by the Santa Lucia nappe in the Jurassic.

The $^{40}Ar/^{39}Ar$ step-heating experiments presented here, combined with microstructural observations and mineral chemistry data, indicate that the Mafic Complex and the Diorite–Granite Complex underwent different tectonothermal evolutions after their intrusion, at ca. 280–285 Ma. The preservation of Permian ages of 277.6 ± 1.3 Ma in sub–magmatic Fe-hornblende and pargasite, which overlap with the intrusion age of the protolith estimated at 279.8 ± 1.4 Ma with U–Pb on zircon (Paquette et al., 2003), indicates that the Diorite–Granite Complex cooled rapidly after its intrusion, then residing at temperatures at which argon diffusion away from the amphibole I crystal lattice was negligible. This thermal history contrasts with the evolution inferred for the Mafic Complex, where granulite facies amphiboles cooled rapidly below 500–600 °C only at 165.4 ± 1.7 Ma. The latter estimate is in line with the Sm–Nd ages of 195 ± 9 Ma obtained from metapelitic septa, interpreted as dating cooling of the Mafic Complex at T < 750–800 °C (Rossi et

al., 2006). The different thermal histories inferred for the Mafic Complex and the Diorite–Granite Complex can be reconciled thanks to the evidence of amphibolite to greenschist facies shearing along the Belli Piani shear zone in the Jurassic. The small grain size of syn-kinematic hornblende does not allow direct dating of this shearing event. However, a maximum age of 187.8 ± 1.4 Ma for shearing at T = 710 ± 40 °C is proposed based on the youngest apparent age provided by the mylonitic leucotonalite Z200. The last stages of shearing at amphibolite facies conditions can be indirectly constrained at ca. 165 Ma, thanks to the apparent ages provided by sample SSL17.3, located in the footwall block.

It is worth noticing that the minimum apparent age of amphibole I cores from Z200 is significantly younger (ca. 70 Myr) than the age estimated for amphibole I in sample SSL2, which escaped shearing along the Belli Piani shear zone. Such age discrepancy cannot be attributed to a larger relative quantity of amphibole II in the mineral separate, since green amphibole rims around Amph I porphyroclasts in Z200 are restricted to a few μm. Therefore, the younger $^{40}Ar/^{39}Ar$ age of the porphyroclastic amphibole indicates that amphibole I in Z200 is not a relic of the original magmatic assemblage but rather a metamorphic mineral formed during early shearing along the Belli Piani shear zone in the Upper Triassic at t > 205.6 ± 1.2 Ma. Early shearing at the Triassic–Jurassic boundary is also in accordance with the inferred onset of cooling of the Mafic Complex at T < 750–800 °C (Rossi et al., 2006). The slight decrease of Na content in the M4 site between amphibole porphyroclasts and neoblasts (Table 1 and Fig. 5e) provides a qualitative estimate of the variations of lithostatic pressure during shearing (Brown, 1977 and Okamoto and Toriumi, 2004). As a result, only a minor decrease of the depth of activity of the shear zone at amphibolite facies can be envisaged. Therefore, the Diorite–Granite Complex, which resided in the hangingwall of the Belli Piani shear zone, underwent only minor exhumation during shearing suggesting that, at least locally, no major faults/shear zones were active at shallower crustal levels.

The extent of relative exhumation of the Mafic Complex with respect to the Diorite–Granite Complex is difficult to estimate, due to the lack of Triassic–Jurassic mineral assemblages suitable for P–T estimates both in the footwall and hangingwall of the Belli Piani shear zone. Previous studies estimated a pressure of ~ 0.5 GPa for the intrusion of the Diorite–Granite Complex (Zibra et al., 2012), whereas the Mafic Complex experienced poly-phase decompression under granulite facies conditions at first at P = 0.7 ± 0.1 GPa, then at P = 0.5 GPa (Caby and Jacob, 2000, Libourel, 1988 and Zibra et al., 2010). Based on this data and on the compatibility of shear sense indicators formed from granulite to upper amphibolite facies conditions throughout the area, Zibra et al. (2010) proposed that the Mafic Complex and the Diorite–Granite Complex were already juxtaposed by the end of the Permian. In this context, the Diorite–Granite Complex would have intruded along a late-Paleozoic shear zone, responsible for the granulite facies shear fabrics of the Mafic Complex. Following this suggestion, the Jurassic amphibolite facies shearing documented in this study would simply re-work a pre-existing lithological boundary, without causing significant crustal excision. However, the widely different post-Permian thermal histories inferred for the Mafic Complex and Diorite–Granite Complex are difficult to reconcile with this view, since they would require an unrealistically large thermal gradient in the Jurassic between samples that would have been located less than 2 km apart.

Therefore, the early stages of shearing along the Belli Piani shear zone can be constrained at the Triassic–Jurassic boundary, at the onset of cooling of the Mafic Complex at T < 750–800 °C. The last stages of shearing at amphibolite facies conditions can be indirectly constrained at ca. 165 Ma (Fig. 7). No significant exhumation of the shear zone was recorded during its activity, thereby suggesting that it resided at a broadly constant depth during its activity. This feature suggests that the Belli Piani shear zone was active at a small to negligible dip angle, possibly as a middle crustal decoupling horizon between lower crustal layers undergoing significant thinning and less deformed

middle to upper crustal layers. A less likely interpretation is that this Jurassic structure was part of a shear zone cutting through different crustal levels. Shearing along the Belli Piani shear zone continued to progressively lower temperatures, in the greenschist facies P–T field, with deformation localizing in the uppermost part of the mylonitic belt, now located at the western edge of the Belli Piani SZ. Middle Jurassic shearing was then followed by the intrusion of doleritic dykes (Caby and Jacob, 2000) and by rapid exhumation at the seafloor, through the activity of low-angle detachment faults preserved in the Murato unit (Fig. 7). Low-angle brittle faults capping continental basement rocks have been repeatedly reported from peri-Tethyan distal continental margins preserved in the Alps (Froitzheim and Eberli, 1990, Masini et al., 2011 and Mohn et al., 2012) and in the Pyrenees (Jammes et al., 2009). This type of basement–cover relationship is considered typical of distal continental margins, where the last stages of crustal thinning are accommodated along gently-dipping detachment faults, which are then overlain by syn- to post-rift sediments (e.g. Péron-Pinvidic and Manatschal, 2009).

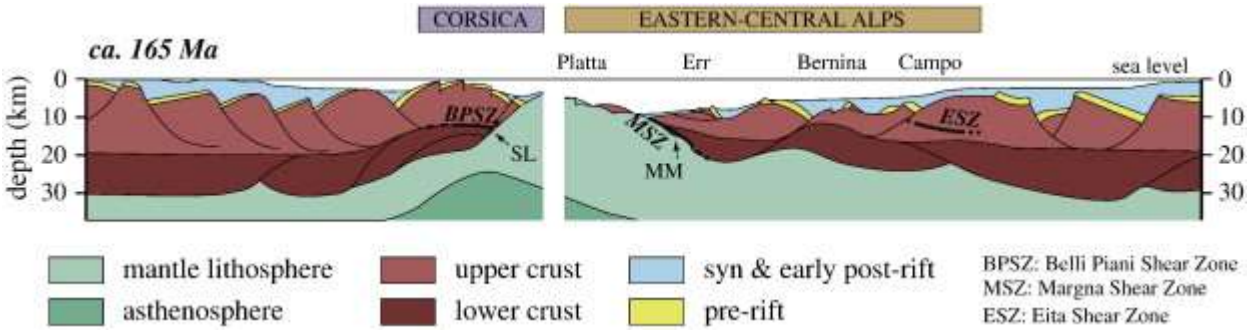

Fig. 7.

Proposed tectonic evolution of the Corsica margin during Middle Jurassic rifting at ca. 165 Ma in the context of the Western Tethys. Note that this section is constructed using Corsica to represent the European margin and the Eastern Central Alps for the Adriatic margin. Shearing along the Belli Piani Shear Zone, which possibly initiated in the Upper Triassic, was still taking place at amphibolite facie conditions at ca. 165 Ma, when the shear zone was sampled in the footwall of exhumation faults. SL = Santa Lucia; MM = Margna–Malenco unit.

Modified from Masini et al. (2013).

6.4. Tectonothermal evolution of distal continental margins in the Western Tethys

The Middle Jurassic Western Tethys oceanic basin is the most studied example of fossil magma-poor rifting worldwide (e.g. Froitzheim and Eberli, 1990, Manatschal, 2004, Manatschal and Müntener, 2009 and Mohn et al., 2010). Thanks to the Alpine orogeny, different sections of the rifted margins are accessible, thereby allowing detailed studies that are complementary to those performed in present-day Atlantic-type margins (e.g. Manatschal, 2004). The distal continental margins that originally surrounded the Western Tethys preserve local evidence of rift-related intra-crustal shear zones, both in the Santa Lucia nappe (this study) and in the Austroalpine units, which sample the distal Adriatic margin [Eita shear zone (Mohn et al., 2012) and Margna shear zone (Bissig and Hermann, 1999)]. Although the existing data set is still relatively small, significant differences in the relative timing of ductile shearing, basement cooling and onset of detachment faulting between the Santa Lucia nappe and the Adriatic marginal units are immediately apparent (Fig. 8).

The Eita shear zone, which was originally located in the necking zone of the Adriatic margin, separates the Campo unit from the overlying Grosina unit (Mohn et al., 2012). This shear zone accommodated the exhumation of the footwall block from middle crustal depth in the 200–185 Ma interval, prior to the onset of activity of low angle detachment faults (Mohn et al., 2012). In a more distal part of the margin, shearing along the Margna shear zone led to the juxtaposition of the lower crustal Fedoz gabbro with upper crustal gneisses (Bissig and Hermann, 1999). The frequent presence of three different amphibole generations within individual samples and the significant Alpine overprint prevent unambiguous dating of the shearing episode, which was interpreted as Upper Triassic to Jurassic (Müntener and Hermann, 2001 and Villa et al., 2000). It is worth noticing that the oldest amphibole generation, which formed through hydration of the granulite facies assemblages of Permian age, yielded minimum ages of ca. 225 Ma ($^{40}Ar/^{39}Ar$ step heating; Villa et al., 2000). This result indicates that amphibole in the Malenco unit was already residing at temperatures below which ^{40}Ar loss is negligible by the Carnian. A similar age of 228 ± 2 Ma ($^{40}Ar/^{39}Ar$ on amphibole), interpreted as due to rift-related cooling along a peri-Tehyan distal continental margin, has also been reported from undeformed mafic granulites in the External Liguride Units of the Northern Apenninnes (Marroni et al., 1998 and Meli et al., 1996).

Differently from the examples discussed above, the last stages of cooling from amphibolite facies conditions in the Santa Lucia nappe took place at ca. 165 Ma. This estimate overlaps within error with the first evidence of mafic magmatism and exhumation of ultramafics at the seafloor preserved in the Alps, Apennines and Corsica (Fig. 8; e.g. Manatschal and Müntener, 2009, Montanini et al., 2006 and Principi et al., 2004). In Corsica, crystallization ages of 169 ± 3 Ma and 161 ± 3 were estimated for trondhjemites in the Balagne nappe (Rossi et al., 2002) and in the Inzecca unit (Ohnenstetter et al., 1981), respectively. MOR-type olivine-gabbro bodies and gabbronorite veinlets from the Monte Maggiore peridotite have been dated at 162 ± 10 Ma and 155 ± 6 Ma (Rampone et al., 2009). Radiolarite ages were constrained in the Balagne nappe at the Upper Bathonian–Early Callovian (Chiari et al., 2000 and Danelian et al., 2008).

This brief review indicates that the rift-related tectonometamorphic evolution of different parts of distal continental margins may be widely different (Fig. 8). In the Western Tethys case study presented here, significant extensional shearing and cooling of middle and lower crustal rocks took place in the Upper Triassic–Lower Jurassic in the units derived from the Adriatic margin. Therefore, progressive cooling and exhumation resulted in an early switch from ductile shear zone-controlled to detachment-dominated crustal thinning (Fig. 8). In the Santa Lucia nappe, instead, this

switch occurred very late in the rifting history and crustal flow was still largely accommodated by amphibolite facies shear zones at ca. 165 Ma.

Further studies will be necessary to determine whether these marked differences may reflect a large scale asymmetry of the evolving lithospheric architecture, which has already been inferred based on the stratigraphic evolution of the conjugate margins (e.g. Masini et al., 2013). In this respect, it is important to note that the original geometric continuity between the Santa Lucia nappe and the Corte slices, which derived from the rift-related Corsica escarpment, has been questioned by recent regional reconstructions (e.g. Molli and Malavieille, 2011). Indeed, similarly to present day magma-poor rifted margins, this margin may have been fragmented, with domains characterized by mantle exhumation and Jurassic magmatism separating the European margin sensu stricto from continental outliers, possibly including the Santa Lucia rocks.

Despite these uncertainties, the Belli Piani shear zone is one of the few shear zones that accommodated rift-related crustal thinning detected worldwide and, most importantly, is the youngest rift-related shear zone found in the Western Tethyan realm.

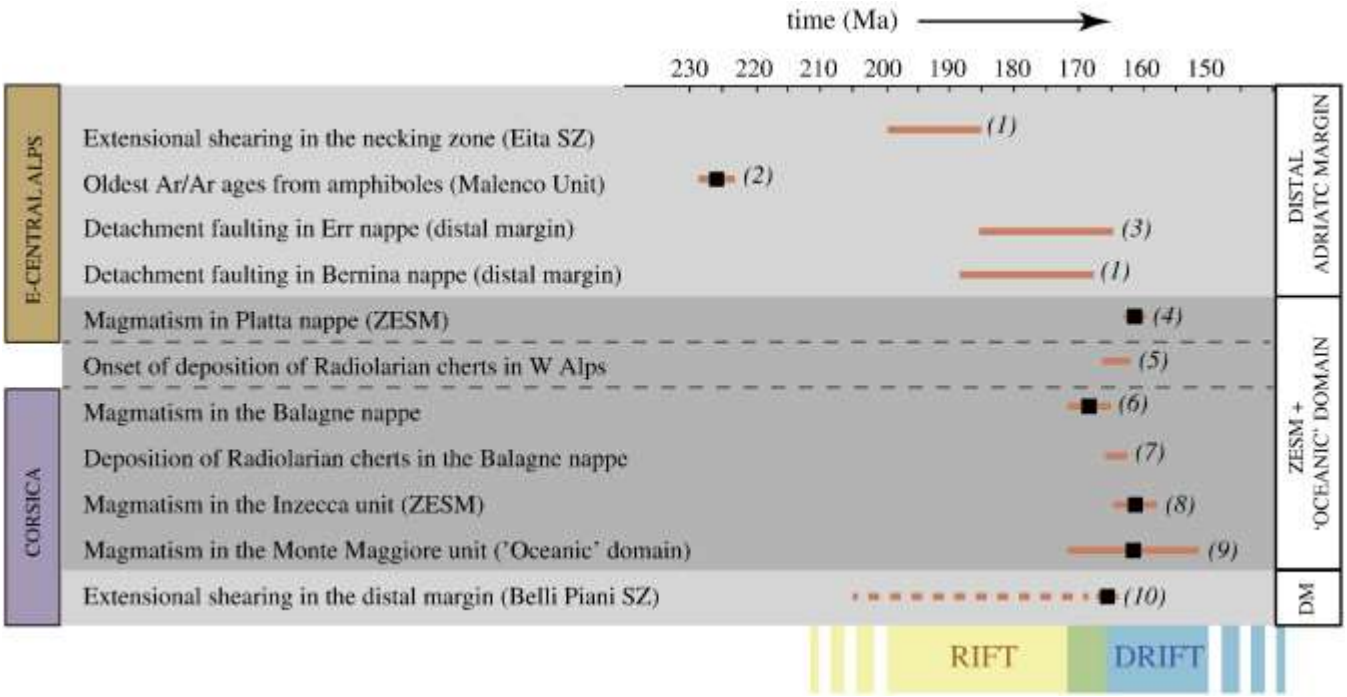

Fig. 8.

Timing of the main tectonic and magmatic events recorded in the distal Adriatic and Corsica margins. Note that the transition from ductile shearing to detachment faulting along the distal Adriatic margin preserved in the Eastern Alps predates breakup by 15–20 Myr. The Santa Lucia unit, instead, preserves evidence for shearing at amphibolite facies conditions at ca. 165 Ma, overlapping with the first evidence of MORB magmatism in the distal-most continental margin and in the Zone of Exhumed Subcontinental Mantle. As a result, widely different thermal gradients were typical of the two distal margins at the rift to breakup transition. References: (1) Mohn et al. (2012); (2) Villa et al. (2000); (3) Masini et al. (2011); (4) Schaltegger et al. (2002); (5) Bill et al. (2001); (6) Rossi et al. (2002); (7) Danelian et al. (2008); (8) Ohnenstetter et al. (1981); (9) Rampone et al. (2009); (10) this study. DM = distal margin.

Acknowledgments

This paper is dedicated to the memory of Piero Elter, for his fundamental and pioneering contribution to the understanding of ocean–continent transition zones. M. Beltrando acknowledges the financial support from the Margin Modelling Phase 3 partners (BP, Conoco Phillips, Statoil, Petrobras, Total, Shell, Hess, BHP-Billiton, BG). R. Tribuzio acknowledges the financial support by Programma di Ricerca di Interesse Nazionale of the Italian Ministero dell'Università e della Ricerca. G. Manatschal, G. Molli, G. Mohn, E. Garzanti and R. Compagnoni are thanked for discussions. S. Sinigoi and an anonymous reviewer are thanked for their comments. M. Marroni is thanked for introducing us to the geology of the Corte Area and for funding of the $^{40}Ar/^{39}Ar$ analyses. Andrea Risplendente is thanked for assistance with the electron microprobe analyses.

References

Afilhado, A., Matias, L., Shiobara, H., Hirn, A., Mendes-Victor, L., Shimamura, H., 2008. From unthinned continent to ocean: the deep structure of the West Iberia passive continental margin at 38°N. Tectonophysics 458, 9–50. http://dx.doi.org/10.1016/j.tecto.2008.03.002

Amaudric Du Chaffaut, S., Caron, J.M., Delcey, R., Lemoine, M., 1972. Données nouvelles sur la stratigraphie des Schistes Lustrés de Corse: la série de l'Inzecca. Comaparaisons avec les Alpes Occidentales et l'Apennin ligure. Comp. Rend. Acad. Sci. Paris D 275, 2611–2614.

Beltrando, M., Lister, G., Forster, M., Dunlap, W.J., Fraser, G., Hermann, J., 2009. Dating microstructures by the $^{40}Ar–^{39}Ar$ step-heating technique: deformation–pressure–temperature–time history of the Penninic Units of the Western Alps. Lithos 113,801–819.

Bill, M., O'Dogherty, L., Guex, J., Baumgartner, P.O., Masson, H., 2001. Radiolarite ages in Alpine–Mediterranean Ophiolites; constraints on the oceanic spreading and the Tethys–Atlantic connection. Geological Society of America Bulletin 113, 129–143.

Bissig, T., Hermann, J., 1999. From pre-Alpine extension to Alpine convergence: the example of the southwestern margin of the Margna nappe (Val Malenco, N-Italy). Schweizerische Mineralogische und Petrographische Mitteilungen 79, 363–380.

Brown, E.H., 1977. The crossite content of Ca-amphibole as a guide to pressure of metamorphism. Journal of Petrology 18, 53–72.

Brun, J.P., Beslier, M.O., 1996. Mantle exhumation at passive margins. Earth and Planetary Science Letters 142, 161–173.http://dx.doi.org/10.1016/0012-821X(96)00080-5.

Caby, R., Jacob, C., 2000. La transition croute-manteau dans la nappe de Santa-Lucia-di-Mercurio (Corse Alpine): les racines d'un rift Permien. Géologie de la France 1, 21–34.

Cebula, G.T., Kunk, M.J., Mehnert, H.H., Naeser, C.W., Obradovich, J.D., Sutter, J.F., 1986. The Fish Canyon Tuff, a potential standard for the $^{40}Ar–^{39}Ar$and fission-track dating methods. Terra Cognita 6, 139.

Chiari, M., Marcucci, M., Principi, G., 2000. The age of radiolarian cherts associated with the ophiolites in the Apennines (Italy) and Corsica (France): a revision. Ofioliti 25,141–146.

Danelian, T., De Wever, P., Durand-Delga, M., 2008. Revised radiolarian ages for the sedimentary cover of the Balagne ophiolites (Corsica, France). Implications for the palaeoenvironmental evolution of the Balano–Ligurian margin. Bulletin de la Societe Geologique de France 179, 289-296.

Di Vincenzo, G., Palmeri, R., 2001. An $^{40}Ar–^{39}Ar$ investigation of high-pressure metamorphism and the retrogressive history of mafic eclogites from the Lanterman Range (Antarctica): evidence against a simple temperature control on argon transport in amphibole. Contributions to Mineralogy and Petrology 141, 15–35.

Dupré, S., Bertotti, G., Cloetingh, S., 2007. Tectonic history along the South Gabon Basin: anomalous early post-rift subsidence. Marine and Petroleum Geology 24, 151–172.
Espurt, N., Callot, J.P., Roure, F., Totterdell, J.M., Struckmeyer, H.I.M., Vially, R., 2012. Transition from symmetry to asymmetry during continental rifting: an example from the Bight Basin–Terre Adélie (Australian and Antarctic conjugate margins).Terra Nova 24, 167–180. http://dx.doi.org/10.1111/j.1365-3121.2011.01055.x.
Froitzheim, N., Eberli, G.P., 1990. Extensional detachment faulting in the evolution of a Tethys passive continental margin, Eastern Alps, Switzerland. Geological Society of America Bulletin 102, 1297–1308.
Froitzheim, N., Schmid, S.M., Conti, P., 1994. Repeated change from crustal shortening to orogen-parallel extension in the Austroalpine units of Graubunden. Eclogae Geologicae Helvetiae 87, 559–612.
Holland, T., Blundy, J., 1994. Non-ideal interactions in calcic amphiboles and their bearing on amphibole–plagioclase thermometry. Contributions to Mineralogy and Petrology116, 433–447.
Huismans, R.S., Beaumont, C., 2008. Complex rifted continental margins explained by dynamical models of depth-dependent lithospheric extension. Geology 36, 163–166.
Huismans, R.S., Beaumont, C., 2011. Depth-dependent extension, two-stage breakup and cratonic underplating at rifted margins. Nature 473, 74–79. http://dx.doi.org/10.1038/nature09988.
Jagoutz, O., Müntener, O., Ulmer, P., Pettke, T., Burg, J.-P., Dawood, H., Hussain, S., 2007. Petrology and mineral chemistry of lower crustal intrusions: the Chilas Complex, Kohistan (NW Pakistan). Journal of Petrology 48, 1895–1953.
Jammes, S., Manatschal, G., Lavier, L., Masini, E., 2009. Tectono-sedimentary evolution related to extreme crustal thinning ahead of a propagating ocean: the example of the western Pyrenees. Tectonics 28.http://dx.doi.org/10.1029/2008TC002406.
Kusznir, N.J., Karner, G.D., 2007. Continental lithospheric thinning and breakup in response to upwelling divergent mantleflow: application to the Woodlark, Newfoundland and Iberia margins. In: Karner, G.D., Manatschal, G., Pinheiro, L.M.(Eds.), Imaging, Mapping and Modelling Continental Lithosphere Extension and Breakup:Geol. Soc. Spec. Publ., 282, pp. 389–419.
http://dx.doi.org/10.1144/SP282.16.
Lavier, L.L., Manatschal, G., 2006. A mechanism to thin the continental lithosphere at magma-poor margins. Nature 440, 324–328. http://dx.doi.org/10.1038/nature04608.
Leake, B.E., Woolley, A.R., Arps, C.E.S., Birch, W.D., Gilbert, M.C., Grice, J.D., Hawthorne, F.C., Kato, A., Kisch, H.J., Krivovichev, V.G., Linthout, K., Laird, J., Mandarino, J., Maresch, W.V., Nickel, E.H., Rock, N.M.S., Schumacher, J.C., Smith, D.C., Stephenson, N.C.N., Ungaretti, L., Whittaker, E.J.W., Youzhi, G., 1997. Nomenclature of amphiboles; report of the Subcommittee on Amphiboles of the International Mineralogical Association Commission on new minerals and mineral names. Mineralogical Magazine 61, 295–321.
Libourel, G., 1985. Le complexe de Santa Lucia di Mercurio (Corse). Ph.D. Thesis, Toulouse University (France).
Libourel, G., 1988. Le complexe de Santa-Lucia di Mercurio (Corse): un nouveau jalon de la base de la croute varisique en Méditerranée occidentale. Comptes-Rendus de l'Académie des Sciences de Paris 307 (Sér.II), 1067–1073.
Maluski, H., Mattauer, M., Matte, P., 1973. Sur la présence de décrochements alpins en Corse. Comptes-Rendus de l'Académie des Sciences de Paris 276, 709–712.
Manatschal, G., 2004. New models for evolution of magma-poor rifted margins based on a review of data and concepts from West Iberia and the Alps. International Journal of Earth Sciences 93, 432–466.
http://dx.doi.org/10.1007/s00531-004-0394-7.

Manatschal, M., Müntener, O., 2009. A type sequence across an ancient magma-poor ocean–continent transition: the example of the western Alpine Tethys ophiolites.Tectonophysics 473, 4–19.
Marroni, M., Molli, G., Montanini, A., Tribuzio, R., 1998. The association of continental crust rocks with ophiolites in the Northern Apennines (Italy): implications for the continent–ocean transition in the Western Tethys. Tectonophysics 292, 43–66.
Masini, E., Manatschal, G., Mohn, G., Ghienne, J.F., Lafont, F., 2011. The tectono-sedimentary evolution of a supra-detachment rift basin at a deep-water magma-poor rifted margin: the example of the Samedan Basin preserved in the Err nappe in SE Switzerland. Basin Research 23, 652–677.http://dx.doi.org/10.1111/j.1365-2117.2011.00509.x.
Masini, E., Manatschal, G., Mohn, G., 2013. The Alpine Tethys rifted margins: reconciling old and new ideas to understand the stratigraphic architecture of magma-poor rifted margins. Sedimentology 60, 174–196.http://dx.doi.org/10.1111/sed.12017.111M. Beltrando et al. / Lithos 168-169 (2013) 99–112
McDougall, I., Harrison, T.M., 1999. Geochronology and Thermochronology by the $^{40}Ar/^{39}Ar$ Method. Oxford University Press.
Meli, S., Montanini, A., Thoni, M., Frank, W., 1996. Age of mafic granulite blocks from the External Liguride Units (northern Apennine, Italy). Mem. Sci. Geol. Padova 48, 65–72.
Mohn, G., Manatschal, G., Müntener, O., Beltrando, M., Masini, E., 2010. Unravelling the interaction between tectonic and sedimentary processes during lithospheric thinning in the Alpine Tethys margins. International Journal of Earth Sciences 99, 75–101. http://dx.doi.org/10.1007/s00531-010-0566-6.
Mohn, G., Manatschal, G., Beltrando, M., Masini, E., Kusznir, N., 2012. Necking of continental crust in magma-poor rifted margins: evidence from the fossil Alpine Tethys margins. Tectonics 31.http://dx.doi.org/10.1029/2011TC002961.
Molli, G., 2008. Northern Apennine–Corsica orogenic system: an updated overview. In: Siegesmund, S., Fügenschuh, B., Froitzheim, N. (Eds.), Tectonic Aspects of the Alpine–Dinaride–Carpathian System: Geolog. Soc. London Spec. Publ, 298, pp. 413–442.
Molli, G., Malavieille, J., 2011. Orogenic processes and the Corsica/Apennines geodynamic evolution: insights from Taiwan. International Journal of Earth Sciences. http://dx.doi.org/10.1007/s00531-010-0598-y.
Montanini, A., Tribuzio, R., Anczkiewicz, R., 2006. Exhumation history of a garnet pyroxenite bearing mantle section from a continent–ocean transition (Northern Apennine ophiolites, Italy). Journal of Petrology 47, 1943–1971.
Müntener, O., Hermann, J., 2001. The role of lower crust and continental upper mantle during formation of non-volcanic passive margins: evidence from the Alps. In:
Wilson, R.C.L., et al. (Ed.), Non-Volcanic Rifting of Continental Margins: A Comparison of Evidence from Land and Sea: Geol. Soc. Spec. Publ., 187, pp. 267–288. http://dx.doi.org/10.1144/GSL.SP.2001.187.01.13.
Müntener, O., Hermann, J., Trommsdorff, V., 2000. Cooling history and exhumation of lower-crustal granulite and upper mantle (Malenco, Eastern Central Alps). Journal of Petrology 41, 175–200.
Ohnenstetter, M., Ohnenstetter, D., Vidal, P., Cornichet, J., Hermitte, D., Mace, J., 1981. Cristallization and age of zircon from Corsican ophiolitic albitites: consequences for oceanic expansion in Jurassic time. Earth and Planetary Science Letters 54, 397–408.
Okamoto, A., Toriumi, M., 2004. Optimal mixing properties of calcic and subcalcic amphiboles' application of Gibbs' method to the Sanbagawa schist, SW Japan. Contributions to Mineralogy and Petrology 146, 529–545.
Osmundsen, P.T., Ebbing, J., 2008. Styles of extension offshore mid-Norway and impli-

cations for mechanisms of crustal thinning at passive margins. Tectonics 27,TC6016. http://dx.doi.org/10.1029/2007TC002242.
Paquette, J.L., Ménot, R.P., Pin, C., Orsini, J.P., 2003. Episodic and short-lived granitic pulses in a post-collisional setting: evidence from precise U–Pb zircon dating through a crustal cross-section in Corsica. Chemical Geology 198, 1–20.
Péron-Pinvidic, G., Manatschal, G., 2009. The final rifting evolution at deep magma-poor passive margins from Iberia–Newfoundland: a new point of view. International Journal of Earth Sciences 98, 1581–1597. http://dx.doi.org/10.1007/s00531-008-0337-9.
Principi, G., Bortolotti, V., Chiari, M., Cortesogno, L., Gaggero, L., Marcucci, M., Saccani, E., Treves, B., 2004. The pre-orogenic volcano-sedimentary covers of the Western Tethys oceanic basin: a review. Ofioliti 29, 177–211.
Puccinelli, A., Perilli, N., Cascella, A., 2012. Stratigraphy of the Caporalino-Sant'Angelo unit: a fake Jurassic–Eocene succession of the"Alpine" Corsica. Rivista Italiana di Paleontologia e Stratigrafia 118, 471–491.
Rampone, E., Hofmann, A.W., Raczek, I., 2009. Isotopic equilibrium between mantle peridotite and melt: evidence from the Corsica ophiolite. Earth and Planetary Science Letters 288, 601–610.
Rieuf, M., 1980. Etude stratigraphique et structurale des unités au nord est de Corte (Corse). Thèse 3e cycle, Toulouse, 211 pp.
Rossi, P., Durand-Delga, M., Caron, J. M., Guieu, G., Conchon, O., Libourel, G., Loÿe-Pilot, M. D., 1994. Notice esplicative, Carte géol. France (1/50000), feuille Corte (1110). Orléans: BRGM, 1454, 150 pp.
Rossi, P., Cocherie, A., Lahondere, D., Fanning, M., 2002. La marge européenne de la Téthys jurassique en Corse: datation de trondhjémites de Balagne et indices de croûte continentale sous le domaine Balano-Ligure. Comptes Rendus Geosciences 334, 313–322.
Rossi, P., Cocherie, A., Fanning, C.M., Deloule, E., 2006. Variscan to Eo-Alpine events recorded in European lower-crust zircons sampled from the French Massif Central and Corsica, France. Lithos 87, 235–260.
Schaltegger, U., Desmurs, L., Manatschal, G., Müntener, O., Meier, M., Frank, M., Bernoulli, D., 2002. The transition from rifting to seafloor spreading within a magma-poor rifted margin: field and isotopic constraints. Terra Nova 14, 156–162.
Speranza, F., Villa, I.M., Sagnotti, L., Florindo, F., Cosentino, D., Cipollari, P., Mattei, M., 2002. Age of the Corsica–Sardinia rotation and Ligure–Provencal Basin spreading:new paleomagnetic and $^{40}Ar/^{39}Ar$ evidence. Tectonophysics 347, 231–251.
Staudacher, T.H., Jessberger, E.K., Dorflinger, D., Kiko, J., 1978. A refined ultrahigh-vacuum furnace for rare gas analysis. J. Phys. E: Sci. Instrum. 11, 781–784.
Steven, T.A., Mehnert, H.H., Obradovich, J.D., 1967. Age of volcanic activity in the San Juan Mountains, Colorado. U.S. Geological Survey Professional Paper 575-D, 47–55.
Tribuzio, R., Renna, M.R., Braga, R., Dallai, L., 2009. Petrogenesis of Early Permian olivine-bearing cumulates and associated basalt dykes from Bocca di Tenda (Northern Corsica): implications for post-collisional Variscan evolution. Chemical Geology 259, 190–203.
Villa, I.M., Hermann, J., Muntener, O., Trommsdorff, V., 2000. $^{40}Ar/^{39}Ar$ dating of multiply zoned amphibole generations (Malenco Italy). Contributions to Mineralogy and Petrology 140, 363–381.
Vitale Brovarone, A., Beltrando, M., Malavieille, J., Giuntoli, F., Tondella, E., Groppo, C.,Beyssac, O., Compagnoni, R., 2011. Inherited ocean–continent transition zones in deeply subducted terranes: insights from Alpine Corsica. Lithos 124. http://dx.doi.org/10.1016/j.lithos.2011.02.013.

Vitale Brovarone, A., Beyssac, O., Malavieille, J., Molli, G., Beltrando, M., Compagnoni, R., 2013. Stacking of continuous segments of subducted lithosphere in high-pressure orogens: architecture of Alpine Corsica (France). Earth-Science Reviews 116, 35–56.

Waters, C.N., 1990. The Cenozoic tectonic evolution of Alpine Corsica. Journal of the Geological Society of London 147, 811–824.

Whitmarsh, R.B., Wallace, P.J., 2001. The rift-to-drift development of the west Iberia nonvolcanic continental margin: a summary and review of the contribution of Ocean Drilling Program Leg 173. Proceedings of the Ocean Drilling Program, Scientific Results.TexasAMUniversity,OceanDrillingProgram,CollegeStation,TX,USA,p.173.

Whitmarsh, R.B., Manatschal, G., Minshull, T.A., 2001. Evolution of magma-poor continental margins from rifting to seafloor spreading. Nature 413, 150–154. http://dx.doi.org/10.1038/35093085.

Wijbrans, J.R., McDougall, I., 1986. $^{40}Ar/^{39}Ar$ dating of white micas from an Alpine high-pressure metamorphic belt on Naxos (Greece): the resetting of the argon isotopic system. Contributions to Mineralogy and Petrology 93, 187–194.

Wilson, R.C.L., Manatschal, G., Wise, S., 2001. Rifting along nonvolcanic passive margins: stratigraphic and seismic evidence from the Mesozoic successions of the Alps and western Iberia. In: Wilson, R.C.L., et al. (Ed.), Non-Volcanic Rifting of Continental Margins: A Comparison of Evidence from Land and Sea: Geol. Soc. Spec. Publ., 187, pp. 429–452.

Zhu, J., Qiu, X., Kopp, H., Xu, H., Sun, Z., Ruan, A., Sun, J., Wei, X., 2012. Shallow anatomy of a continent–ocean transition zone in the northern South China Sea from multichannel seismic data. Tectonophysics 554–557, 18–29. http://dx.doi.org/10.1016/j.tecto.2012.05.027.

Zibra, I., 2006. Late-Hercynian granitoid plutons emplaced along a deep crustal shear zone. A case study from the S. Lucia Nappe (Alpine Corsica, France). Ph.D. Thesis, Pisa University (Italy). The complete manuscript is available from:http://etd.adm.unipi.it/theses/available/etd-09142006-171856/.

Zibra, I., Kruhl, J.H., Braga, R., 2010. Late Palaeozoic deformation of post-Variscan lower crust: shear zone widening due to strain localization during retrograde shearing. International Journal of Earth Sciences 99, 973–991.

Zibra, I., Kruhl, J.H., Montanini, A., Tribuzio, R., 2012. Shearing of magma along a granulite-facies shear zone: evolution of microstructures during the transition from magmatic to solid-stateflow. Journal of Structural Geology 37, 150–160.